Multiband counterparts of two eclipsing ultraluminous X-ray sources in M 51

R. Urquhart,[1]★ R. Soria,[1,2,3]★ H. M. Johnston,[3] M. W. Pakull,[4] C. Motch,[4]
A. Schwope,[5] J. C. A. Miller-Jones[1] and G. E. Anderson[1]

[1]*International Centre for Radio Astronomy Research, Curtin University, GPO Box U1987, Perth, WA 6845, Australia*
[2]*National Astronomical Observatories, Chinese Academy of Sciences, Beijing 100012, China*
[3]*Sydney Institute for Astronomy, School of Physics A28, The University of Sydney, Sydney, NSW 2006, Australia*
[4]*Observatoire astronomique, Université de Strasbourg, CNRS, UMR 7550, 11 rue de l'Université, F-67000 Strasbourg, France*
[5]*Leibniz-Institut für Astrophysik Potsdam, An der Sternwarte 16, D-14482 Potsdam, Germany*

ABSTRACT

We present the discovery and interpretation of ionized nebulae around two ultraluminous X-ray sources in M 51; both sources share the rare property of showing X-ray eclipses by their companion stars and are therefore prime targets for follow-up studies. Using archival *Hubble Space Telescope* images, we found an elongated, 100-pc-long emission-line structure associated with one X-ray source (CXOM51 J132940.0+471237; ULX-1 for simplicity), and a more circular, ionized nebula at the location of the second source (CXOM51 J132939.5+471244; ULX-2 for simplicity). We observed both nebulae with the Large Binocular Telescope's Multi-Object Double Spectrograph. From our analysis of the optical spectra, we argue that the gas in the ULX-1 bubble is shock-ionized, consistent with the effect of a jet with a kinetic power of $\approx 2 \times 10^{39}$ erg s^{-1}. Additional X-ray photoionization may also be present, to explain the strength of high-ionization lines such as He II $\lambda 4686$ and [Ne V] $\lambda 3426$. On the other hand, the emission lines from the ULX-2 bubble are typical for photoionization by normal O stars suggesting that the nebula is actually an H II region not physically related to the ULX but is simply a chance alignment. From archival Very Large Array data, we also detect spatially extended, steep-spectrum radio emission at the location of the ULX-1 bubble (consistent with its jet origin), but no radio counterpart for ULX-2 (consistent with the lack of shock-ionized gas around that source).

Key words: accretion, accretion discs – stars: black holes – X-rays: binaries.

1 INTRODUCTION

Ultraluminous X-ray sources (ULXs) are off-nuclear, compact accreting X-ray sources with luminosities greater than those of Galactic stellar-mass black holes (see Kaaret, Feng & Roberts 2017 and Feng & Soria 2011 for reviews). They exceed the Eddington limit for a standard 10 M$_{\odot}$ black hole ($L_x \gtrsim 10^{39}$ ergs^{-1}) and are thought to be the result of either supercritical accretion on to stellar-mass compact objects or sub-critical accretion on to intermediate-mass black holes (IMBHs). Some of the brightest ULXs may contain IMBHs (Farrell et al. 2009); however, the consensus has moved towards super-Eddington stellar-mass accretors for most ULXs. The discovery of three neutron star ULXs (Bachetti et al. 2014;

Fürst et al. 2016, 2017; Israel et al. 2017a,b) has strengthened this interpretation.

Being highly energetic sources, ULXs have a significant impact on their surroundings. Their extreme X-ray luminosity photoionizes the surrounding gas. Examples of ULX nebulae with a dominant X-ray photoionized component are Holmberg II X-1 (Pakull & Mirioni 2002) and NGC 5408 X-1 (Kaaret et al. 2003; Soria et al. 2006). The ionizing X-ray luminosities inferred from the optical line emission of these nebulae match (within a factor of a few) the apparent X-ray luminosities of the compact objects, suggesting that at least those ULXs are not strongly beamed and their luminosities are intrinsically high (e.g. Pakull & Mirioni 2002, 2003; Kaaret & Corbel 2009). In addition to high photon luminosity, there is theoretical and observational evidence of powerful outflows (winds or jets) in ULXs (Ohsuga et al. 2005; Ohsuga & Mineshige 2011; Pinto, Middleton & Fabian 2016), consistent with their nature as supercritical accretors. The kinetic power of the outflows

★E-mail: ryan.urquhart@icrar.org (RU); roberto.soria@curtin.edu.au (RS)

produces shock-ionized nebulae (ULX bubbles), such as those around IC 342 X-1 (Cseh et al. 2012) or Holmberg IX X-1 (Miller 1995; Grisé, Pakull & Motch 2006; Pakull, Grisé & Motch 2006). Tell-tale signs of the presence of shock-ionized gas are the expansion velocity of the bubble ($\sim$100–300 km s^{-1}) and the high [S$_{II}$]/Hα line ratio; in fact, some ULX bubbles were previously mistakenly identified as supernova or hypernova remnants. In most cases, photoionized and shock-ionized gas co-exist in a ULX bubble; the origin of the ionizing photons may be both the direct emission from the central object and the forward shock precursor.

In a small number of shock-ionized ULX bubbles, there is also direct evidence of collimated jets instead of (or in addition to) wide-angle outflows. The evidence is the elongated morphology of the bubble with symmetrical hot spots or lobes/ears. In particular, this is seen in NGC 7793-S26 (Pakull, Soria & Motch 2010; Soria et al. 2010) and M 83-MQ1 (Soria et al. 2014). In both cases, the X-ray luminosity from the central source is less than the ULX threshold ($\approx 10^{39}$ erg s^{-1}), either because our direct view of the source is mostly obscured, or because the instantaneous accretion rate is currently low. It is their kinetic power ($P_{jet} > 10^{39}$ erg s^{-1}), inferred from the expansion velocity of the shocked gas and from the optical/IR line emission of the bubble (Pakull et al. 2010), that puts those three sources in the class of supercritical accreting stellar-mass objects. Another well-known ULX bubble, MF16 in NGC 6946 (Roberts & Colbert 2003; van Dyk et al. 1994), has an elongated morphology consistent with the propagation of a symmetrical jet into the interstellar medium (ISM); in that case, the direct X-ray luminosity of the central source does exceed the ULX threshold, but may still be only a small part of the bolometric luminosity, mostly reprocessed in the *UV* band (Kaaret et al. 2010).

Evidence of powerful jets has also been found in a few other ULXs that do not have optically bright, shock-ionized hot spots/lobes. In the ultraluminous supersoft source M 81 ULS-1, the jet is revealed by the red and blue Doppler shifts of its Balmer emission lines, corresponding to $v \approx 0.17c$ (Liu et al. 2015). The M 81 source is classified as an ultraluminous supersoft source, because of its thermal spectrum with blackbody temperature of $\approx$80 eV (Swartz et al. 2002). The presence of a collimated jet in that source suggests that jets can co-exist with thick winds, which are likely to be the hallmark of the supersoft class (Poutanen et al. 2007; Soria & Kong 2016; Urquhart & Soria 2016a); however, no evidence of jets has been found so far in other sources of that type.

More often, it is bright radio emission with 5-GHz luminosity $\nu L_\nu \gtrsim 10^{34}$ erg s^{-1} that indicates the presence of a jet or at least of fast outflows. The reason is that some of the bulk kinetic energy of the outflow is used to accelerate relativistic electrons at the reverse shock; compression of the magnetic field lines in the shocked ISM leads to electron cooling via synchrotron radiation (Begelman, Blandford & Rees 1984). In Holmberg II X-1, the jet is revealed by a flaring radio core and radio-bright 'knots' of synchrotron emission either side of the core (Cseh et al. 2014, 2015). The three extragalactic sources with elongated optical bubbles mentioned above (NGC 7793-S26, M 83-MQ1, NGC 6946-MF16) all have strong optically thin synchrotron emission. By analogy, the equally strong, optically thin radio nebula (diameter $\approx$ 40 pc; Lang et al. 2007) around NGC 5408 X-1 is also interpreted as evidence of a jet. The strong radio source associated with NGC 5457 X-9 (Mezcua et al. 2013a) could be another example, although in that case it is difficult to disentangle the ULX contribution from the surrounding H$_{II}$ region. In addition, a candidate IMBH microquasar in NGC 2276 has a 5-GHz luminosity of 7×10^{37} erg s^{-1} and a linear size of 650 pc (Mezcua et al. 2013b, 2015). In the Milky Way, SS 433 very

likely belongs to the same class of jetted, supercritical sources with extended bubbles and mechanical power $\gtrsim 10^{39}$ erg s^{-1} (Zealey, Dopita & Malin 1980; Fabrika 2004; Brinkmann et al. 2007; Goodall, Alouani-Bibi & Blundell 2011; Farnes et al. 2017); in that source, tell-tale signatures of the large-scale jet impact on to the ISM are the radio 'ears' protruding out of the W 50 bubble (Dubner et al. 1998) and the characteristic optical line emission from filaments of shock-ionized gas (Boumis et al. 2007).

Not every optically bright, shock-ionized ULX bubble has a radio counterpart (NGC 1313 X-2 is a classical example of a large, optically bright, radio-quiet ULX bubble), and not every ULX with a bright radio counterpart is surrounded by an optically bright, shock-ionized bubble (as we said for Holmberg II X-1). For a given kinetic power in the jet, the composition of the jet (leptonic or baryonic), the collimation angle, the nature of the compact object, the gas density and magnetic field strength in the ISM, and the age of the bubble may affect the fraction of kinetic power that goes into synchrotron cooling. In other cases, such as the radio flares detected in the transient M 31 ULX (Middleton et al. 2013), the jet may be active only for a short fraction of time during state transitions; this is in contrast with sources such as NGC 7793-S26 where the average jet power is $\sim$ several 10^{40} erg s^{-1} over $\sim 10^5$ yr (Pakull et al. 2010).

We are conducting a study of ULXs associated with ionized nebulae in nearby galaxies, trying to determine which of them have evidence of jets, and whether the presence of a jet correlates with some X-ray spectral properties of the central source. We have recently identified (Urquhart & Soria 2016b) two ULXs in the same spiral arm (Fig. 1) of the interacting galaxy M 51 ($d = 8.58 \pm 0.10$ Mpc; McQuinn et al. 2016). The most intriguing property of those two sources is that both of them show sharp X-ray eclipses, likely due to occultations by their respective companion stars. For the first source, M 51 ULX-1, we were able to determine that the period is either $\approx$6–6.5 d, or $\approx$12–13 d; we did not detect enough eclipses to identify the period of the second source, M 51 ULX-2, but we estimated $P \sim 10$ d based on its eclipse fraction (Urquhart & Soria 2016b). Both ULXs have similar luminosities ($L_X \approx$ a few 10^{39} ergs^{-1}), must be viewed at high inclination (being eclipsing sources), and are likely to be located in ISM regions with similar properties (as they are only $\sim$400 pc apart along the same arm); however, they have different X-ray spectral characteristics (Urquhart & Soria 2016b). In this paper, we show that both ULXs are surrounded by ionized gas. In one case (M 51 ULX-1), the ULX is coincident with an elongated 'jet-like' bubble. The other ULX (M 51 ULX-2) is surrounded by a quasi-circular bubble. We will argue that in ULX-2 the nebula is consistent with an ordinary H$_{II}$ region photoionized by young stars, while in ULX-1, the gas is shock ionized and the morphology suggests a jet origin. We will also show that the candidate jet source has a radio counterpart, while the other ULX does not.

2 OBSERVATIONS AND DATA REDUCTION

2.1 Archival *HST* images

Publicly available *Hubble Space Telescope* (*HST*) data for M 51 were downloaded from the Hubble Legacy Archive.[1] The observations were part of the *HST* Mosaic of M 51 (proposal ID 10452) taken on 2005 January 12 with the Advanced Camera for Surveys (ACS), Wide Field Channel (WFC). This data set includes three
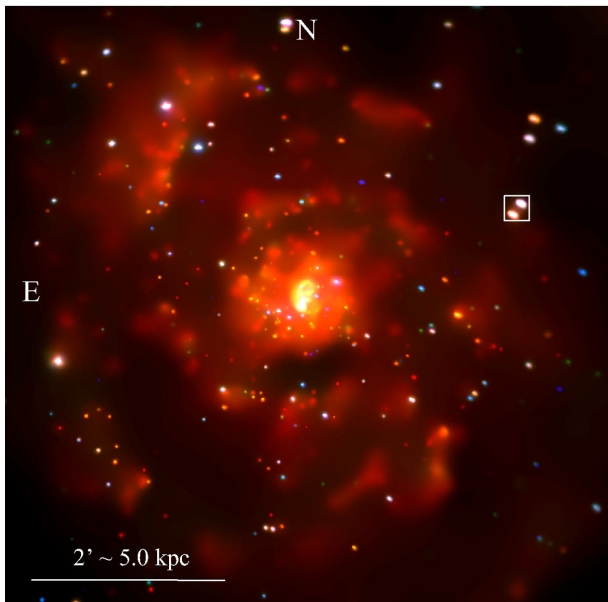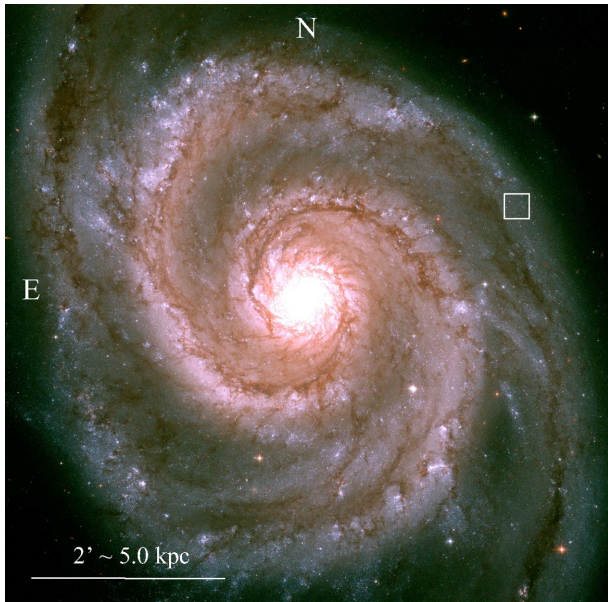
---

[1] http://hla.stsci.edu/hlaview.html

Figure 1. Top panel: *HST*/ACS-WFC RGB colour image of M 51. Blue represents the F435W filter, green represents F555W and red represents F814W. The 15 arcsec × 15 arcsec white box contains ULX-1 and ULX-2 and shows the region in which we performed PSF photometry. Bottom panel: *Chandra*/ACIS X-ray colour image, on the same scale as the *HST* image. Red = 0.3–1 keV, green = 1–2 keV, and blue = 2–7 keV. Inside the box, ULX-1 is the lower source (softer colour), while ULX-2 is the upper source (harder colour).

broad-band filters (F435W, F555W, and F814W) and the narrow-band filter F658N, which covers H α and the two adjacent [N$_{II}$] lines (central wavelength of 6584 Å and effective width of 75 Å). The total exposure time for the F814W and F555W bands was 8160 s, while for F435W it was 16 320 s and for F658N 15 640 s. The archival data were processed 'on-the-fly' using the standard ACS pipeline (CALACS: Hack & Greenfield 2000), correcting for flat-fielding, bias and dark current. We then built a normalized, weighted average of the images in the F814W and F555W bands, and subtracted it from the F658N image, in order to remove the continuum stellar
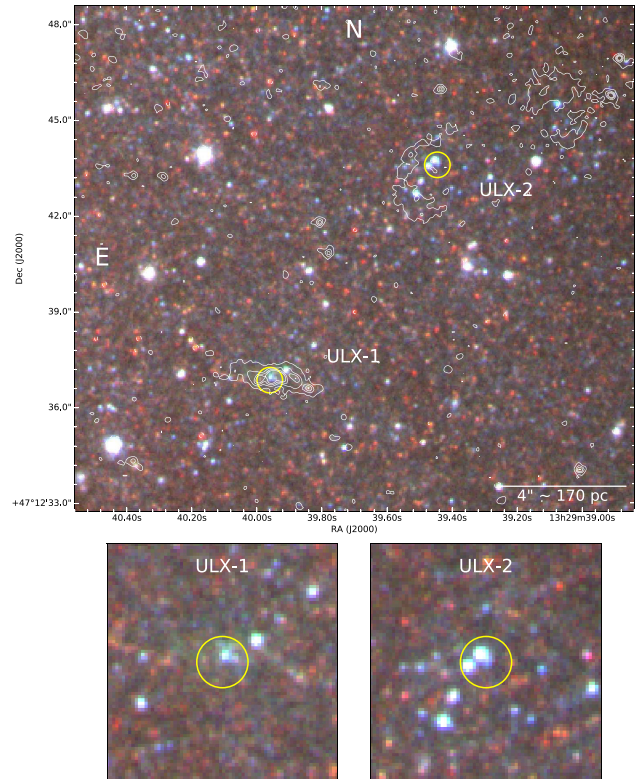

Figure 2. Top panel: zoomed-in *HST*/ACS image of the white box displayed in Fig. 1. Blue represents the F435W band, green = F555W, and red = F814W. Yellow circles represent the *Chandra* positions of ULX-1 and ULX-2 with 0.4 arcsec errors. White contours represent optical line emission in the continuum-subtracted F658N band. Line emission can be seen near both ULXs; in ULX-1 there is an elongated jet-like structure while ULX-2 is inside a more spherical nebula. Contours levels are arbitrary and are simply used to indicate the morphology of the ionized gas nebulae. Bottom left-hand panel: zoomed-in view of the ULX-1 field. Bottom right-hand panel: zoomed-in view of the ULX-2 field.

contribution from the narrow-band filter. Henceforth, when we refer to the F658N image, we mean the continuum-subtracted image unless stated otherwise.

We performed aperture and point-spread function (PSF) photometry on the F435W, F555W and F814W filters, using the DAOPHOT package (Stetson 1987) embedded within the Image Reduction and Analysis Facility (IRAF) software Version 2.16 (Tody 1993). The *daofind* task was used to identify point-like sources within a 50 arcsec × 50 arcsec region centred on the mid-point between ULX-1 and ULX-2 (a concentric region approximately four times larger than the white box in Fig. 1). Aperture photometry was then performed on these stars using *phot*. Due to the crowded nature of the field (Fig. 2), a circular source aperture with a radius of 3 pixels (0.15 arcsec) was used; the encircled energy fraction within that radius, for a point-like source, is ≈80 per cent. For the PSF photometry, several bright, isolated sources were manually selected and inspected (with the tasks *pstselect* and *psf*); each candidate PSF star was manually inspected and those that appeared slightly extended were rejected. The average PSF created from those stars was then used as input to the photometry task *allstar*. PSF photometry was conducted on all stars within a 15 arcsec ×15 arcsec box centred on the mid-point of ULX-1 and ULX-2 (white box overplotted in Fig. 1 and displayed in its entirety in Fig. 2). In addition to the
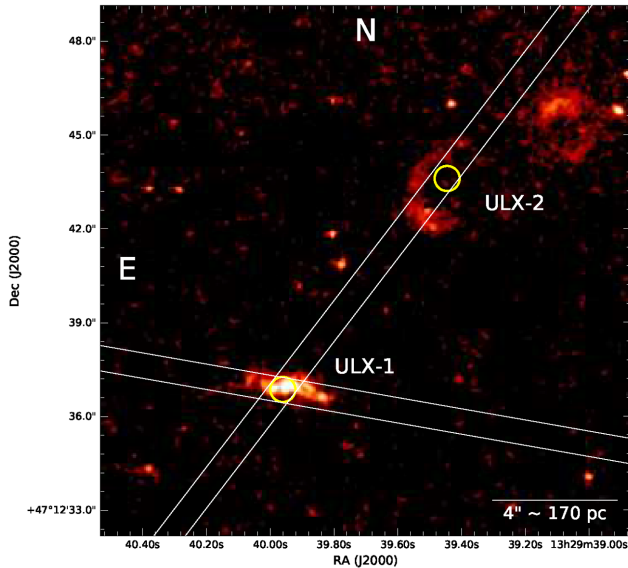
Figure 3. LBT slit positions, overplotted on the continuum-subtracted F658N image. In the first observation, the slit was aligned along the jet-like structure near ULX-1, including also the candidate optical counterpart of the ULX. This corresponded to an instrument celestial position angle of 80° east of north. The second slit was positioned so as to observe the candidate optical counterparts of both ULX-1 and ULX-2, along with some of the diffuse emission around the two X-ray sources. This corresponded to a position angle of 322.5°. The yellow circles represent the *Chandra* positions of ULX-1 and ULX-2 with 0.4 arcsec uncertainty.

photometry of point-like sources, we measured the total background-subtracted count rates of the emission nebulae around the two ULXs. Finally, count rates of stellar and nebular sources were converted to physical magnitudes and fluxes in the various bands, using the zero-point tables for ACS-WFC available on the STScI web site.[2]

2.2 New Large Binocular Telescope spectra

Optical spectroscopic data together with the corresponding calibration exposures (dark and bias frames, flat-fields, arcs) were taken with the Large Binocular Telescope's (LBT) Multi-Object Double Spectrograph (MODS; Pogge et al. 2010). The targets were observed from 2016-05-10 UTC 06:31:53.064 (MJD 57518.272142) for a total of $3 \times 900 = 2700$ s, on each of the two MODS, and for each of two slit positions. We used a 0.8 arcsec wide, segmented long slit with gratings G400L and G670L for the blue and red beam channels, respectively. The blue G400L grating has a resolution of 1850 at 4000 Å and a nominal dispersion of 0.5 Å per pixel, while the red G670L has a resolution of 2300 at 7600 Å and nominal dispersion of 0.8 Å per pixel. In the first observing configuration (OB1), the slit was oriented along the jet-like structure of ULX-1 [position angle (PA) = 80°, measured from north to east]; in the second configuration (OB2), the slit was oriented to contain both the (candidate) point-like optical counterparts of ULX-1 and ULX-2 (Fig. 3), at PA = 322.5°.

The raw data were bias-subtracted and flat-fielded with the reduction package modsCCDRed[3] Version 2.0.1, provided by Ohio State University. Spectral trimming and wavelength calibration were done with the Munich Image Data Analysis System (MIDAS; Warmels 1992). We then used standard IRAF tasks for further analysis. We extracted one-dimensional background-subtracted spectra with the IRAF task *apall*. We flux-calibrated the red and blue spectra using the response files provided by the MODS instrumentation team. Finally, we analysed the spectra using the IRAF task *splot*; in particular, for each emission line, we measured equivalent width (EW), full width at half-maximum (FWHM), and central wavelength (by fitting a Gaussian profile).

One of the main parameters we were interested in was the total Hα flux from the elongated nebula around ULX-1. The LBT slit was placed and oriented in order to cover as much of that region as possible (Fig. 3), but some of the flux (about 20 per cent) falls out of the slit. However, we can measure the total emission of that nebula from the *HST* F658N image, which includes the flux from Hα plus [N II] λ6548 and [N II] λ6583. We combined the information on the Hα/[N II] line ratio obtained from the LBT spectra, with the measurement of the total Hα + [N II] flux from the *HST* image. This gave us an absolute measurement of the total Hα luminosity of the nebula, regardless of what fraction of it falls on the LBT slit. After calibrating the Hα flux, we then obtained the fluxes of all other emission lines in both the red and the blue spectrum, using their ratios to Hα. (In other words, we assumed as a first-order approximation that the same fraction of total flux was collected in the red and blue spectra.) We applied a similar procedure to determine the total Hα flux (and by extension, the fluxes in the other lines) of the nebula around ULX-2, which could only be partly covered by the 0.8 arcsec LBT slit (Fig. 3). Finally, we de-reddened the spectra assuming line-of-sight extinction $A_V = 0.095$ mag corresponding to $E(B - V) = 0.031$ mag (Schlafly & Finkbeiner 2011), using the extinction curves of Cardelli, Clayton & Mathis (1989). We chose to correct only for the line-of-sight Galactic extinction as a simple, model-independent, standard reference value. We are aware that there must additional extinction intrinsic to M 51, but it is difficult to quantify it. The total dust reddening of the nebulae is likely less than or similar to the value indirectly inferred from X-ray spectral fitting of the two ULXs inside the nebulae (Urquhart & Soria 2016b), that is $E(B - V)_{int} \lesssim 0.1$ mag; a plausible guess is that the intrinsic extinction through the M 51 halo is similar to the extinction through the Milky Way halo, that is the total A_V is about twice the Galactic line-of-sight value.

An additional caveat is that MODS does not have an Atmospheric Dispersion Corrector, so the spectral data suffer from slit losses due to atmospheric dispersion, when the slit is not fixed at or near the parallactic angle. Normalizing the Hα line flux to the value inferred from the *HST* image allows us to sidestep this problem, at least for the red spectra. We used the Ohio State University's online calculator[4] to estimate the effect that differential atmospheric refraction may have on our MODS spectra. The observations with the slit in the OB1 configuration were taken at an hour angle $\approx 0^h9$–1^h2; the differential refraction between Hα and Hβ is $\lesssim 0.2$ arcsec. For the OB2 configuration, the spectra were taken at hour angles $\approx 2^h2$–2^h5, corresponding to differential refractions ≈ 0.3 arcsec between Hα and Hβ and 0.4 arcsec between Hα and Hγ.

This shift is already of the same size as the typical spatial scale of structural inhomogeneities (brighter and fainter clumps) in the two nebulae; therefore, in principle, a fraction of nebular emission may be on the slit at H α but fall outside the slit at bluer wavelengths. We will argue a posteriori, from our results, that the uncertainty on the total extinction and on the effect of differential refraction are small and do not affect our interpretation.

2.3 Archival VLA data

Radio maps of M 51 were provided by G. Dumas (private communication); see Dumas et al. (2011) for a detailed discussion of the instrumental set-up. In summary, observations were taken from 1998 to 2005 using the Very Large Array (VLA) at 1.4 GHz (20 cm) in the A, B, C, and D configurations, at 4.9 GHz (6 cm) in the B, C, and D configurations, and at 8.4 GHz (3.6 cm) in the C and D configurations. A total integration time of ∼170 hr over all three frequencies was achieved. The 8.4 and 4.9 GHz observations had been combined with data from the Effelsberg 100-m telescope (Dumas et al. 2011) to detect extended emission regions that are resolved out in the VLA maps. The synthesized beam sizes for the 8.4, 4.9, and 1.4 GHz are 2.4, 2.0, and 1.5 arcsec, respectively. Radio fluxes were determined using the Astronomical Imaging Processing System (AIPS; Greisen 2003). We fitted elliptical Gaussian profiles in the image plane, using the task imfit to determine the integrated flux of the detected sources; we also calculated peak fluxes and root-mean-square noise levels in the field around the ULXs. We placed 3σ upper limits on non-detections.

2.4 Astrometric alignment

In order to identify any optical and/or radio candidate counterparts of ULX-1 and ULX-2, we first needed to verify and, if necessary, improve the astrometric alignment between the *Chandra*, *HST*, and VLA images. For our first iteration, we took the default *Chandra* astrometry of the re-processed and stacked archival data. The X-ray data were processed and analysed with standard tasks within the Chandra Interactive Analysis of Observations (CIAO) Version 4.7 (Fruscione et al. 2006); for a description of the *Chandra* observations, see Urquhart & Soria (2016b). The *Chandra*/ACIS-S astrometry is known to be accurate within ≈0.5 arcsec for 68 per cent of the observations, and within ≈0.7 arcsec for 90 per cent of the observations.[5] The *HST* astrometry was aligned on to the 2MASS catalogue (Skrutskie et al. 2006), which provides an accuracy within 0.3 arcsec. The VLA astrometry was assumed absolutely correct by default. With this first set of astrometric solutions, we looked for coincidences between the X-ray, optical, and radio sources (not including the ULXs that were the subject of our study), within 0.5 arcsec.

The positions of the X-ray sources were determined with the CIAO task wavdetect; the optical centroids of point-like sources with profile fitting in the DS9 package (Joye & Mandel 2003); the radio positions with the AIPS package imfit. We found seven coincidences between X-ray and optical point-like sources, four coincident optical and radio sources, and four X-ray/radio coincidences. From a comparison of the optical/X-ray and optical/radio coincidences, we noticed that the *HST* astrometry was systematically offset by 0.′′1 in both RA and Dec; therefore, we corrected the *HST* astrometry by that amount. The revised *HST* astrometry is still within the 0.3 arcsec uncertainty of the 2MASS catalogue.
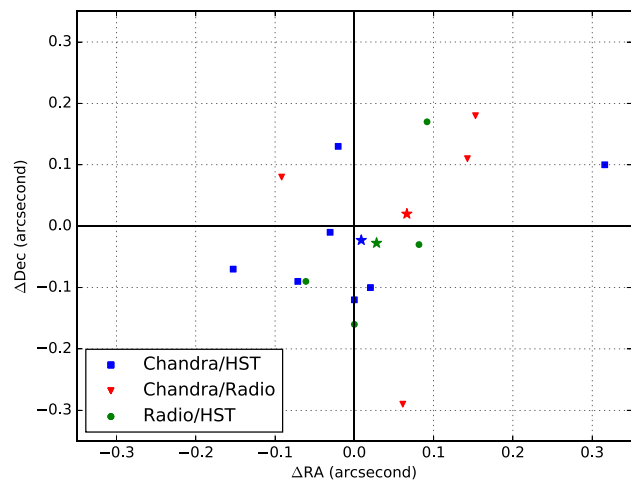
Figure 4. Relative positions of coincident, point-like *Chandra*, *HST*, and VLA/Effelsberg sources. *Chandra* and *HST* coincidences are plotted as blue squares; *Chandra* and radio coincidences as red triangles; *HST* and radio coincidences as green circles. Stars represent the average offset between each pair of bands; systematic offsets are <0.1 arcsec between any pair of bands. The residual discrepancies (<0.4 arcsec) are due to random scatter, mostly because of poor centroid determination of X-ray sources located far from the ACIS aimpoint.

The X-ray positions (based on only four coincidences) were already within 0.1 arcsec of the radio position and also within 0.02 arcsec of the average of the improved *HST* positions. The resulting relative astrometry can be seen in Fig. 4, with the average offsets between the three bands marked by stars. We did not find it necessary to make any further systematic corrections to any band. The residual discrepancies between the bands are simply random scatter of the individual sources. This is mostly due to the fact that the PSF of point-like sources a few arcmin away from the *Chandra*/ACIS aimpoint becomes very extended and elongated, which increases the uncertainty in their central positions. In summary, we adopt the following X-ray positions for our ULXs: RA (J2000) = $13^h29^m39^s.960$, Dec. (J2000) = $+47°12'36''.86$ for ULX-1; RA (J2000) = $13^h29^m39^s.444$, Dec. (J2000) = $+47°12'43''.60$ for ULX-2. For both positions, we estimate a 3σ error radius of 0.4 arcsec, due to their off-axis positions and elongated PSF shape.

3 MAIN RESULTS

3.1 Point-like optical counterparts

For ULX-1, only one bright optical candidate lies within the *Chandra* error circle (Fig. 2, bottom left). This candidate is embedded in the brightest part of the elongated H α nebula (Fig. 3). For ULX-2, there are two potential optical counterparts within the *Chandra* error circle (Fig. 2, bottom right), separated by ≈0.25 arcsec, with comparable brightness and colours. The relatively low precision of the *Chandra* position makes it impossible to rule out either candidate at this stage. The Vegamag brightnesses of the three sources in the *HST* bands (de-reddened for a line-of-sight extinction corresponding to $A_V = 0.095$ mag, with Cardelli extinction law) are summarized in Table 1. At a distance modulus of 29.67 mag, the absolute magnitudes and colours of all three sources are consistent with those of bright giants (luminosity class II) or blue supergiants (class Ib); if two of those three sources are the true counterparts of ULX-1 and ULX-2, they are likely to contain also a

Table 1. De-reddened brightness of the candidate optical counterparts. Brightness values have been corrected for a line-of-sight Galactic reddening $E(B - V) = 0.031$ mag, corresponding to an extinction $A_{F435W} = 0.13$ mag, $A_{F555W} = 0.10$ mag, and $A_{F814W} = 0.06$ mag. All three optical sources are consistent with bright giants (luminosity class II) or supergiants (class Ib), of approximate spectral type B5–B6 for the ULX-1 star, and B3–B4 for the ULX-2 stars.

Source ID	F435W (mag)	F555W (mag)	F814W (mag)
ULX-1	24.62 ± 0.03	24.64 ± 0.05	24.87 ± 0.07
ULX-2 (north)	23.14 ± 0.03	23.33 ± 0.03	23.59 ± 0.03
ULX-2 (south)	23.60 ± 0.04	23.77 ± 0.02	23.87 ± 0.04

contribution from disc emission. For simplicity, we investigate two extreme scenarios; first, purely emission from the stellar companion and second, purely emission from the irradiated disc. It is likely that the true emission is some combination of both processes, and thus we investigate the upper limits of stellar brightness and irradiation in this section.

To constrain the ages of the three sources and of the surrounding stellar population, we used colour–magnitude diagrams in the three *HST* broad-band filters (Fig. 5); we plotted all stars with reliable brightness values within the 15 arcsec ×15 arcsec field shown in Fig. 2. The black arrow in each plot indicates the effect of a hypothetical additional intrinsic extinction $A_V = 1$ mag. We compared the data with a set of theoretical isochrones[6] (Bressan et al. 2012; Chen et al. 2015) for a metallicity $Z = 0.015$ (Fig. 5, top panels) and $Z = 0.040$ (Fig. 5, bottom panels). The choice of those two alternative metal abundances reflects the two discrepant classes of values generally quoted in the literature for the disc of M 51; see e.g. Croxall et al. (2015) and Bresolin, Garnett & Kennicutt (2004) for the argument in favour of slightly sub-solar metallicities, and Moustakas et al. (2010) and Zaritsky et al. (1994) in favour of supersolar values. We will return to this metallicity discrepancy in Section 3.2.2.

Comparing the colour–magnitude plots, we notice that the inferred ages of the optical companion of ULX-1 are not consistent: ≈ 30 Myr in the (F435W–F555W) versus F555W diagram, and ≈ 10–20 Myr in the (F555W–F814W) versus F814W diagram, regardless of metal abundance. The two ages cannot be made consistent with the addition of intrinsic extinction; the star is ≈ 0.15 mag brighter in the F555W band than predicted by stellar isochrones. The reason for this small discrepancy is unclear. We note that the source is embedded in the most luminous part of the optical nebula, with its strong [O III] $\lambda\lambda 4959,5007$ emission lines falling into the F555W band, which makes the subtraction of the local background emission more challenging and may be responsible for the small excess in that band. Alternatively, some of the optical emission from that point-like source is coming from the accretion disc or the outflow around the ULX, so that its colours are slightly different from a pure stellar spectrum. Distinguishing between the optical emission from donor star and accretion flow is a notoriously difficult task in ULXs (Tao et al. 2011, 2012; Grisé et al. 2012; Soria et al. 2012; Gladstone et al. 2013; Heida et al. 2014); we will return to this issue later in this section.

Keeping those caveats in mind, we conclude that the optical counterpart for ULX-1 has a most likely age of ∼20 Myr, if dominated by a single donor star. We also plot stellar density bands (blue

[6] Available at http://stev.oapd.inaf.it/cgi-bin/cmd.

and green shaded regions in Fig. 5). These shaded regions indicate regions of the parameter space where stars have a stellar density consistent with a Roche lobe-overflow binary of period 6 or 12 d, respectively. These two alternative values of the period come from the recurrent eclipses found in the X-ray light curves for ULX-1 (Urquhart & Soria 2016b); the 6-d period is a solution suitable for mass ratios $4 \lesssim q \lesssim 10$, while the 12-d period is the solution corresponding to mass ratios $0.5 \lesssim q \lesssim 1$, where $q \equiv M_2/M_1$. Those two characteristic periods are then converted to stellar densities via the period-density-q relation (Eggleton 1983). The current optical data (taking into account also the possible contamination from disc and nebular emission) are not sufficient to test whether the candidate star sits in either band. Thus, we cannot yet use this method to rule out either of the proposed orbital periods of ULX-1 and constrain its mass ratio. However, we illustrate this method as a proof of concept, and to highlight the fact that the candidate optical star is at least approximately consistent with the kind of Roche lobe-filling donor star required for ULX-1.

For ULX-2, both candidate optical counterparts have ages consistent with ≈ 10 Myr, and mass $M \approx 18 M_\odot$, if we correct for Galactic line-of-sight extinction only. If we also include additional dust reddening within M 51 equal to the Galactic value, the inferred age of both stars is instead ≈ 8 Myr, and their masses $M \approx 22$–$23 M_\odot$. Stars at this evolutionary stage have a characteristic radius $\sim 30 R_\odot$ and a characteristic density $\rho \sim 3 \times 10^{-4}$ g cm^{-3}. This would imply a characteristic binary period of 24 d for $q \approx 1$ (i.e. for the case of a canonical black hole primary), or a period of 10 d for $q \approx 17$ (i.e. for the case of a canonical neutron star primary). The period of ULX-2 could not be directly measured from its X-ray light curve (Urquhart & Soria 2016b) and so we do not have enough observational constraint to test this prediction yet; however, there is at least a plausible hint, from the average eclipse fraction, that the period is ~ 10 d (Urquhart & Soria 2016b), consistent with the neutron star scenario.

From Fig. 5, we can see that both potential ULX-2 optical counterparts appear to be outliers, much brighter and bluer than the surrounding stars. We considered and dismissed the possibility that they are the counterparts of two luminous X-ray sources, unresolved in the *Chandra* image. The reason this is unlikely is that ULX-2 shows sharp, deep eclipses, during which the residual luminosity is $L \approx 3 \times 10^{37}$ erg s^{-1}. Barring implausible coincidences, this must be the upper limit to the luminosity of any potential second X-ray source. Such a luminosity would not be enough to contribute significantly to the optical emission, via reprocessing of X-ray irradiation, given that both optical sources have $M_V \sim -6$ mag. Thus, we conclude that at least one of the two blue point-like sources in the *Chandra* error circle for ULX-2 is an intrinsically bright star, while the other source may either be dominated by irradiation, or also be an intrinsically bright donor star.

Next, we try to quantify whether X-ray irradiation can significantly contribute to the optical counterpart of ULX-1 and to one of the two blue stars at the location of ULX-2. The X-ray spectrum of ULX-1 is well fitted by an irradiated disc model (Urquhart & Soria 2016b), for example the XSPEC model *diskir* (Gierliński, Done & Page 2009). In Fig. 6, we plot the combined X-ray spectrum and optical data points, together with a sequence of *diskir* models with varying levels of reprocessing ($f_{out} = 0.1$, 0.05, 0.01, and 0.005). If we want to explain the optical flux as the intercepted and reprocessed component of the X-ray flux, we need a reprocessing fraction $f_{out} \approx 0.075$. This is an order of magnitude higher than predicted (Vrtilek et al. 1990; de Jong, van Paradijs & Augusteijn 1996; King, Kolb & Szuszkiewicz 1997; Dubus et al. 1999) or observed (Hynes
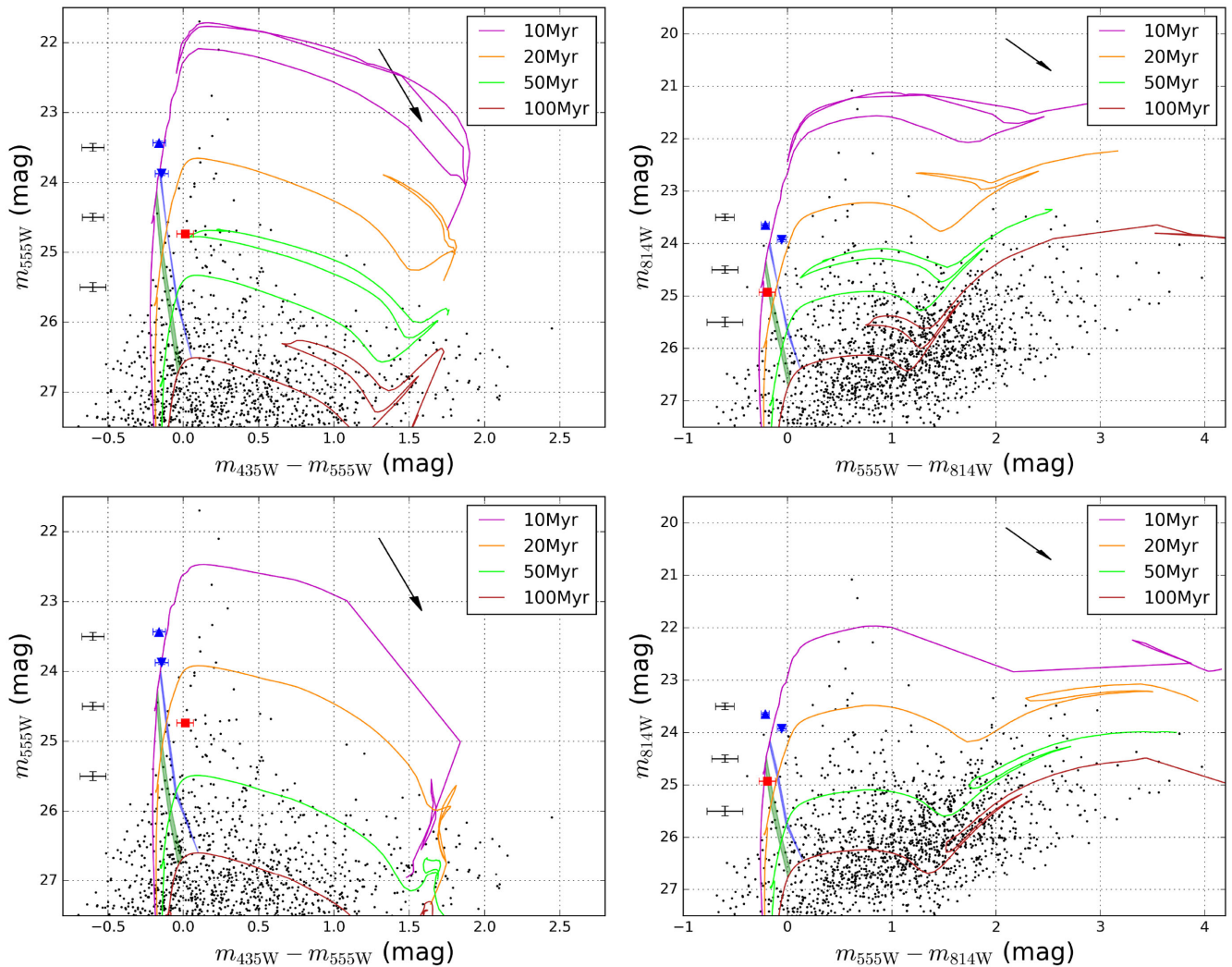
Figure 5. Top left-hand panel: colour–magnitude diagram in the (F435W–F555W) versus F555W bands. The red square represents the candidate optical counterpart of ULX-1. The blue triangle represents the northern candidate counterpart for ULX-2, while the upside-down blue triangle represents the southern candidate counterpart. Black data points show the surrounding stars, with the black error bars on the left indicating their average uncertainties for each F555W magnitude interval. The black arrow shows the effect of one magnitude of extinction in F555W. Overlaid are Padova stellar isochrones for metallicity $Z = 0.015$. The isochrones have been corrected for a line-of-sight extinction $A_V = 0.095$ mag. The green and blue vertical bands drawn across the isochrones represent the expected brightness and colour of Roche lobe-filling stars with stellar densities consistent with a binary period of 6 or 12 d, respectively, as seen in the X-ray light curve of ULX-1 (see Section 3.1). Top right-hand panel: as in the top left-hand panel, but for F555W–F814W versus F814W. Bottom left-hand panel: as in the top left-hand panel, but with Padova stellar isochrones corresponding to a metallicity $Z = 0.040$. Bottom right-hand panel: as for the top right-hand panel, but for $Z = 0.040$.

et al. 2002; Gierliński et al. 2009; Russell et al. 2014) in Galactic X-ray binaries with sub-Eddington standard discs, although Gandhi et al. (2010) found that the reprocessing fraction could be as high as 20 per cent in the Galactic black hole binary GX 339-4. However, much less is known about the reprocessing fraction in ULXs. For a transient ULX in M 83, Soria et al. (2012) estimated a reprocessing fraction of $f \approx 5 \times 10^{-3}$; for other ULXs, reprocessing fractions of a few 10^{-2} were inferred (Sutton, Done & Roberts 2014). Supercritical accreting sources have geometrically thicker discs in the inner region, but even so, the disc alone cannot directly intercept such a high fraction of the X-ray emission; however, if the ULX has a broad disc outflow and polar funnel geometry, some of the X-ray photons emitted along the funnel may be scattered by the wind and irradiate the outer disc (Sutton, Done & Roberts 2014; Narayan, Sądowski & Soria 2017). Indeed, we argued (Urquhart &

Soria 2016b) that ULX-1 may have a strong wind, because of its soft X-ray spectral residuals, which in other ULXs are associated with outflows (Middleton et al. 2015; Pinto et al. 2016). Nonetheless, we also know that ULX-1 must have a fairly large donor star, because of its eclipses, and we have already shown that the inferred size of the star is roughly consistent with the observed optical flux. Alternatively, the non-simultaneity of the X-ray and optical data may contribute to the unphysically high reprocessing fraction that is required. However, studying the long- and short-term X-ray variability of ULX-1 (and ULX-2) from *Chandra*, *XMM–Newton,* and *Swift*,[7] we find that the source only varies by a factor of ≈ 2. Any

---

[7]For *XMM–Newton* and *Swift*, ULX-1 and ULX-2 are unresolved and thus we can only study their combined variability.
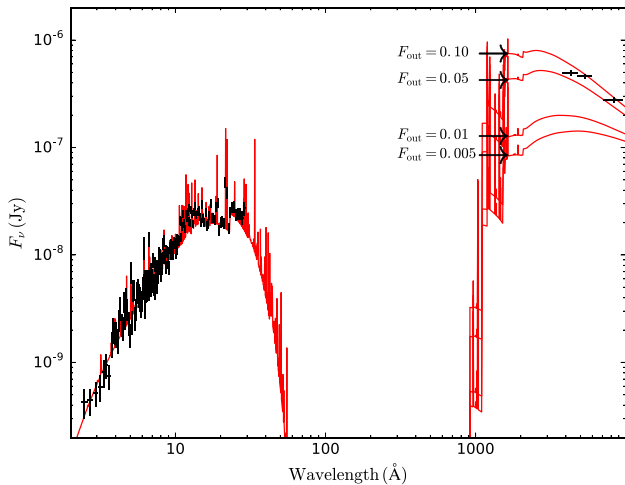
Figure 6. Stacked *Chandra*/ACIS-S spectrum and *HST* data points (black) for ULX-1, fitted with a *diskir* plus thermal plasma models (red curves). A sequence of four models has been plotted, differing only for their optical reprocessing fraction $f_{\rm out}$. A very high reprocessing fraction (almost 10 per cent) is formally required in this model to reproduce the high optical/X-ray flux ratio. Such a high value strongly suggests that we are seeing a significant contribution to the optical continuum flux from the donor star, although we cannot separate the disc and star components with the data at hand.

change in the optical flux (assuming irradiation of the disc) must be less than that amount, because the optical emission comes from the Rayleigh–Jeans tail of the disc spectrum and it includes an intrinsic non-variable contribution from the stellar companion. We can use a similar argument for ULX-2. In that case, the best-fitting XSPEC model to the X-ray spectrum reported by Urquhart & Soria (2016b) is a *diskpbb* model (slim disc) rather than *diskir*, so we cannot directly constrain the reprocessing fraction from the model parameters. However, forcing a fit of the same spectrum with *diskir* we obtain a reprocessing fraction ≈ 0.2; this is because the observed X-ray flux is approximately the same as from ULX-1, while the optical flux is three times brighter. That makes it even more difficult to explain the optical emission as dominated by an irradiated disc rather than by a supergiant donor star.

3.2 Ionized nebulae

The *HST*/ACS image in the continuum-subtracted F658N filter clearly shows the presence of line emission around both ULXs (Figs 2 and 3). The nebula around ULX-1 is elongated, with a length of ≈ 2.5 arcsec ≈ 100 pc and a width of ≈ 0.7 arcsec ≈ 30 pc. The nebula around ULX-2 is more circular, with an outer radius of ≈ 1.6 arcsec ≈ 65 pc. There is also another region of line emission ≈ 200 pc to the north-west of ULX-2, of similar size and brightness, but without any bright X-ray source inside. In the absence of other evidence, we assume that this nebula is unrelated to ULX-2, rather than (for example) being part of a double-lobed structure powered by the ULX.

We defined source and background regions suitable for the two nebulae, and extracted their net count rates. We obtain rates of 21.52 ± 0.10 and 12.79 ± 0.25 ct s^{-1} for the ULX-1 and ULX-2 nebulae, respectively, in the F658N band. We then used the *HST*/ACS zero-point tables available online[8] (see also Bohlin 2016) to con-

[8] https://acszeropoints.stsci.edu/

vert count rates to fluxes. A count rate of 1 ct s^{-1} corresponds to a flux of $\approx 1.95 \times 10^{-18}$ erg cm^{-2} s^{-1} Å^{-1} in that band. The effective width of the filter is 75 Å. Thus, the integrated line fluxes from the two nebulae are $(3.39 \pm 0.02) \times 10^{-15}$ erg cm^{-2} s^{-1} and $(2.01 \pm 0.04) \times 10^{-15}$ erg cm^{-2} s^{-1}, respectively, where we have also applied a de-reddening correction for line-of-sight extinction. At a distance of 8.6 Mpc, this corresponds to line luminosities of $\approx 3.0 \times 10^{37}$ erg s^{-1} and $\approx 1.8 \times 10^{37}$ erg s^{-1}, respectively, in the F658N filter. The filter bandpass covers [N II] $\lambda 6548$, Hα $\lambda 6563$, and [N II] $\lambda 6583$. Those three lines are redshifted by $\Delta \lambda \approx 9$ Å with respect to their rest-frame wavelengths, because of the systemic velocity of M 51. This ensures that the flux from the [N II] $\lambda 6548$ line is entirely included in the F658N bandpass, given the moderate line widths that we will discuss later in this section. Of course, the *HST* image alone cannot tell us how the line flux is split between Hα and the [N II] lines. For this, we need to examine the LBT spectra.

The LBT spectra across the ULX-1 and ULX-2 nebulae are displayed in Figs 7 and 8, respectively. The emission lines significantly detected in the two spectra, and their flux ratios to Hβ, are listed in Table 2. Those values are the total emission from the whole of each nebula. We recall that we obtain the total flux of each line by rescaling the Hα + [N II] flux measured in the LBT spectrum to the total flux measured from the *HST* image in the F658N filter, and then rescaling the LBT fluxes of every other line according to their ratios to Hα. We also recall that ULX-1 was observed both in the OB1 (slit along the bubble) and OB2 (slit across the bubble) configurations. To a first approximation, the two spectra are identical; in this paper, we use the spectra for the OB1 slit, because they provide a better approximation to the average emission of the whole nebula. A more comprehensive comparison of the two spectra and of the internal structure of the ULX-1 nebula is left to the further work.

From the line ratios (Table 2), we find Balmer decrements Hα : Hβ = 2.99 ± 0.14, Hγ : Hβ = 0.46 ± 0.03 in the ULX-1 nebula; in the ULX-2 nebula, Hα : Hβ = 3.07 ± 0.15, Hγ : Hβ = 0.30 ± 0.02. The canonical values for case B recombination are 2.87:1:0.47 at 10 000 K and 2.75:1:0.48 at 20 000 K (Osterbrock & Ferland 2006). However, the Balmer decrement is slightly steeper for radiative shocks: for solar metallicity and a shock velocity of 150 km s^{-1}, the ratios are 3.06:1:0.46, while for a shock velocity of 500 km s^{-1}, the Balmer decrement is 2.92:1:0.47 (Allen et al. 2008). Thus, the observed Balmer decrement in the ULX-1 nebula is perfectly consistent with shock-ionized gas. Instead, for the ULX-2 nebula, the observed decrement is steeper than expected. Part of the reason for the discrepancy may be that a few per cent of the flux in the bluer part of the spectrum is lost (compared with the flux in the red spectrum) because of differential refraction, as we mentioned in Section 2.2; this affects particularly Hγ and particularly the ULX-2 spectrum because of the slit orientation in the OB2 configuration (Section 2.2). In addition, we have only corrected for line-of-sight extinction; if we add an intrinsic dust reddening comparable to the Galactic reddening (Section 2.2), the extinction-corrected Hα : Hβ ratio is reduced by 4 per cent and the Hγ : Hβ ratio is increased by 3 per cent. Overall, those small uncertainties do not affect our main results and interpretation of the spectra. In the rest of this section, we focus on the most significant properties of the two nebulae, and their main differences.

3.2.1 ULX-1 nebula

We see strong [N II] and [S II] lines relative to Hα (Fig. 7), with a flux ratio ([N II] $\lambda 6548$ + [N II] $\lambda 6583$)/H$\alpha \approx 1.7$ and ([S II] $\lambda 6716$ + [S II] $\lambda 6731$)/H$\alpha \approx 0.81$. Such high ratios (even after accounting for a
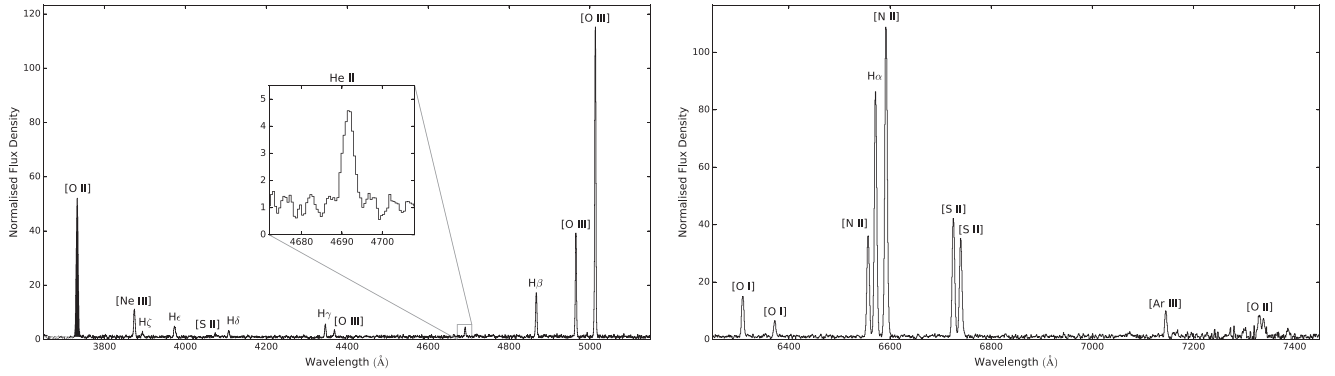
Figure 7. Left-hand panel: LBT MODS1 plus MODS2 spectrum (blue arm) of the nebula around ULX-1, normalized to the continuum. The spectrum comes from the OB1 slit configuration (PA $= 80°$), which is along the long axis of the jet-like nebula. Inset: zoomed-in view of the He II λ4686 emission line. Right-hand panel: as in left-hand panel, but for the red side of the spectrum. (Note the different flux density scales of the two panels.)
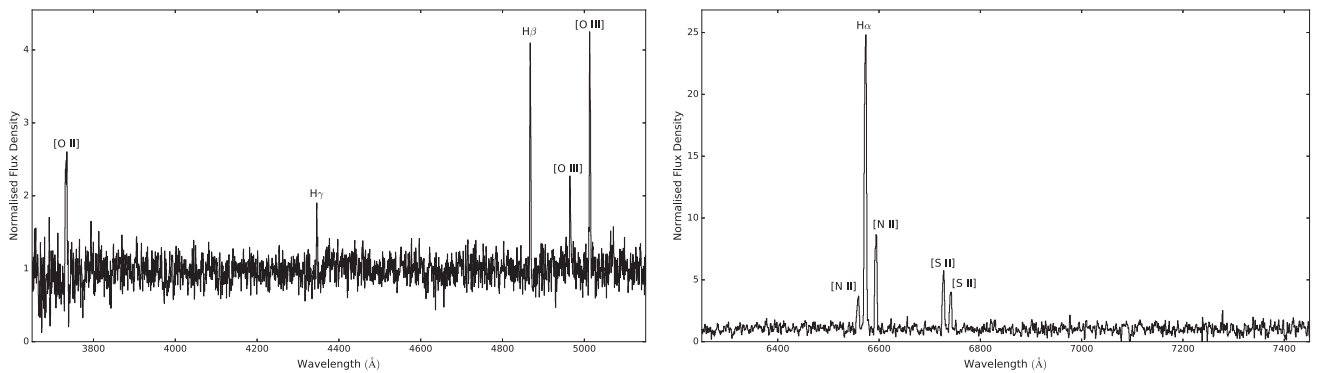

Figure 8. Left-hand panel: LBT MODS1 plus MODS2 spectrum (blue arm) of the nebula around ULX-2, normalized to the continuum. The spectrum comes from the OB2 slit configuration (PA $= 322°.5$); the stellar continuum includes both candidate optical counterparts of ULX-2. Right-hand panel: as in the left-hand panel, but for red side of the spectrum. (Note the different flux density scales of the two panels.)

possible supersolar abundance in the disc of M 51) are traditionally good indicators of shock-ionized material (Mathewson & Clarke 1973; Blair & Long 1997; Gordon et al. 1998). Based on those ratios alone, the bubble could be classified as a typical supernova remnant; however, its very elongated morphology and the presence of a ULX in the middle make it more likely that the gas is shocked by a jet emitted from the compact object, as is the case in other ULX bubbles. The ULX-1 bubble also shows He II λ4686 (Fig. 7) and [N v] λ3426 (Table 2) emission. Both features are consistent with shock-ionized gas and/or X-ray photoionized gas, but are not consistent with stellar photoionization.

In order to estimate the electron temperature and density of the gas, we used standard diagnostic line ratios (Osterbrock 1989), coded in the task temden in IRAF (Shaw & Dufour 1994). For the [O III] line (sensitive to electron temperature), we measure an intensity ratio $I(\lambda4959 + \lambda5007)/I(\lambda4363) \approx 35$, which corresponds to $T_e[\text{O III}] = 22\,000 \pm 2000$ K. From the [O II] line intensity ratio $I(\lambda3726 + \lambda3729)/I(\lambda7320 + \lambda7330) \approx 12$, we measure $T_e[\text{O II}] = 20\,000 \pm 1000$ K. (In general, those two temperature values do not need to agree, as they may be due to emission coming from different regions.) Those temperatures are a factor of 2 higher than expected for typical H II regions, and suggest that there is a significant component of shock-ionized gas. For the [S II] line (sensitive to electron density), we find an intensity ratio [S II] $I(\lambda6716)/I(\lambda6731) \approx 1.20$. Around the previously estimated values of T_e, this ratio corresponds to $n_e = (280 \pm 60)$ cm^{-3}. This is to be interpreted as the density of

the compressed gas behind the shock, much higher than the density of the undisturbed ISM, typically ~ 1 cm^{-3} in the spiral arms of a galaxy.

From the de-reddened Hβ flux, at the distance of M 51, we calculate an emitted luminosity $L_{\text{H}\beta} \approx 3.7 \times 10^{36}$ erg s^{-1}. Knowing the characteristic temperature and density of the emitting gas, and using the Hβ volume emissivity for case B recombination (Osterbrock 1989), we infer an emitting volume $V_e \approx 8 \times 10^{56}$ cm^3. This is much lower than the volume inferred from the appearance of the nebula in the *HST* image, that is (roughly) an elongated bubble with a size of $\approx 30 \times 100$ pc corresponding to a volume of $\approx 10^{60}$ cm^3. Such a discrepancy is expected for a shock-ionized bubble, because the line-emitting gas occupies only a very thin layer behind the shock. For the inferred density and volume of the shocked layer, the mass of currently line-emitting gas is ~ 200 M$_\odot$. The total gas mass originally present in the 10^{60} cm^3 region that has now been swept up in the bubble must have been $\sim 10^3$ M$_\odot$ for ISM densities ~ 1 cm^{-3}. The cooling time-scale of the shocked gas from the immediate, hot post-shock temperature ($T > 10^6$ K) to the warm temperature range in which most of the optical line emission is produced ($T \sim 10^4$ K) is $\sim 10^4$ yr, and that is followed by a short recombination time-scale ($\approx 10^3$ yr) of the warm gas (Dopita & Sutherland 2003); on the other hand, typical ages of shock-ionized ULX bubbles are $\sim 10^5$ yr. Thus, it is likely that much of the gas that passed through the shock has already cooled, even if the ULX is continually supplying radiative and kinetic power.

Table 2. Extinction-corrected emission line fluxes for the nebulae around ULX-1 and ULX-2, inferred from our LBT spectra and scaled by the *HST* images. Fluxes were corrected for a line-of-sight extinction $A_V = 0.095$ mag. All fluxes were re-normalized so that the Hα + [N II] fluxes match the corresponding line fluxes measured from the *HST* image. Fluxes are displayed in terms of their strength relative to the Hβ line ($100 F_\lambda / F_{H\beta}$).

Line	$100 \times (f_\lambda / f_{H\beta})$	
	ULX-1	ULX-2
3426 [Ne V]	16 ± 1	
3728 [O II] ($\lambda 3726 + \lambda 3729$)	605 ± 28	88 ± 6
3726 [O II][a]	243 ± 11	
3729 [O II][a]	353 ± 16	
3869 [Ne III]	92 ± 5	
3889 Hζ + He I	17 ± 2	
3967 [Ne III] + Hϵ $\lambda 3970$	47 ± 2	
4069 [S II][b]	22 ± 5	
4104 Hδ	24 ± 2	
4340 Hγ	46 ± 3	30 ± 2
4363 [O III]	23 ± 2	
4686 He II	22 ± 1	
4861 Hβ	100	100
4959 [O III]	207 ± 10	30 ± 3
5007 [O III]	604 ± 28	96 ± 5
5200 [N I] ($\lambda 5198 + \lambda 5202$)	15 ± 1	
6300 [O I]	66 ± 3	
6364 [O I]	24 ± 2	
6548 [N II]	127 ± 6	48 ± 2
6563 Hα	299 ± 14	307 ± 15
6583 [N II]	377 ± 19	95 ± 5
6716 [S II]	132 ± 6	51 ± 3
6731 [S II]	111 ± 5	35 ± 3
7136 [Ar III]	21 ± 1	
7320 [O II]	51 ± 4	
9069 [S III]	20 ± 1	
9532 [S III]	40 ± 3	
10049 H I Pa α	3.0 ± 0.2	
12818 H I Pa β	2.2 ± 0.3	
Hβ flux (10^{-16} erg cm^{-2} s^{-1})	4.21 ± 0.18	4.47 ± 0.17

Notes.[a]Deblended with IRAF line-fitting tools.
[b]Slightly contaminated by [S II] $\lambda 4076$.

We then investigated whether the lines are broad or narrow. From the bright night-sky lines [O I] $\lambda 5577$ and Hg I $\lambda 4358$, we find an instrumental full width at half-maximum FWHM$_{ins,b}$ = 2.95 Å for the blue spectrum. In the red spectrum, strong night-sky lines are seen at $\lambda = 6329$ Å, $\lambda = 6498$ Å, $\lambda = 6863$ Å: from the average width of those lines, we measure FWHM$_{ins, r}$ = 4.76 Å. The intrinsic line width FWHM$_{int}$ is obtained from the observed width FWHM$_{obs}$, following the relation FWHM$_{int}$ = (FWHM$_{obs}^2$ − FWHM$_{ins}^2$)$^{1/2}$. Gaussian fits to the Hβ and Hα line profiles give observed FWHM$_{obs}$ of ≈3.7 and 4.0 Å, respectively, corresponding to intrinsic widths of 140 ± 20 km s^{-1} and 110 ± 20 km s^{-1}. Other low-ionization lines have similar intrinsic widths: 115 ± 20 km s^{-1} for [O I] $\lambda 6300$, 115 ± 20 km s^{-1} for [N II] $\lambda\lambda 6548, 6583$, and 130 ± 20 km s^{-1} for [S II] $\lambda\lambda 6716, 6731$. Thus, all low-ionization lines are significantly resolved and are indicative of a shock velocity $v_s \approx$ FWHM$_{int}$ ≈ 110–130 km s^{-1}. Further evidence of line broadening is obtained from the intrinsic half-width at zero-intensity (HWZI) for the Balmer lines; we measure HWZI(Hα) ≈ 280 km s^{-1}, and HWZI(Hβ) ≈ 250 km s^{-1}. On the other hand, somewhat unexpectedly, high-ionization lines are slightly narrower than low-ionization ones. Both [O III] $\lambda 4959$ and [O III] $\lambda 5007$ have intrinsic FWHMs = 90 ± 5 km s^{-1} and HWZI ≈ 200 km s^{-1}. He II $\lambda 4686$ is even

narrower, with an intrinsic FWHM = 60 ± 20 km s^{-1} and HWZI ≈ 180 km s^{-1}.

Finally, we examined the more characteristic line ratios. A detailed modelling of the spectrum is beyond the scope of this paper; however, here we highlight the presence and strength of the high ionization lines [Ne V] $\lambda 3426$, with $I(\lambda 3426)/I(H\beta) = 0.16 \pm 0.01$, and He II $\lambda 4686$, with $I(\lambda 4686)/I(H\beta) = 0.22 \pm 0.01$. Neither of those lines can be produced at such intensity by a relatively slow (≈120 km s^{-1}) shock plus precursor. The combined presence of [Ne V] $\lambda 3426$ and He II $\lambda 4686$ is the most intriguing feature of some ultracompact dwarf galaxies (Izotov, Thuan & Privon 2012); the origin of the lines in those galaxies was unclear, but the most likely candidates were suggested to be fast radiative shocks or an AGN contribution. In M 51 ULX-1, we have the rare opportunity to identify a source of such line emission. Moreover, the emission from [Ne III] $\lambda 3869$, [O III] $\lambda 4959, 5007$, and [N II] $\lambda 6548, 6583$ is remarkably strong, with $I(\lambda 3869)/I(H\beta) = 0.92 \pm 0.05$, $I(\lambda 4959)/I(H\beta) = 2.1 \pm 0.1$ and $I(\lambda 6548)/I(H\beta) = 1.27 \pm 0.05$. If entirely due to shock-ionization, those line ratios are approximately consistent only with shock velocities ~500–600 km s^{-1}. Based on the shock plus precursor models of Allen et al. (2008), at this range of velocity, these line ratios are only weakly dependent on the unperturbed ISM density, metal abundance and magnetic field. We do not see such high-velocity wings in the LBT spectra; however, this could be due to our viewing angle of the collimated outflow in the plane of the sky, with the direction of the fast outflow almost perpendicular to our line of sight.

3.2.2 ULX-2 nebula

The spectrum of the nebula around ULX-2 (Table 1 and Fig. 8) is clearly different from that of the ULX-1 nebula. From an analysis of the line width, we find that all lines are consistent with the instrumental widths (see Section 3.2.1, Fig. 9). That is evidence that the gas is photoionized rather than shock ionized. The [N II] and [S II] lines are much weaker, relative to Hα, with flux ratios ([N II] $\lambda 6548$ + [N II] $\lambda 6583$)/Hα ≈ 0.47 and ([S II] $\lambda 6716$ + [S II] $\lambda 6731$)/Hα ≈ 0.28. This is again consistent with a photoionized H II region.

Again we tried using standard diagnostic line ratios for temperature and density. Unfortunately, the [O III] $\lambda 4363$ line is too faint to provide meaningful temperature constraints. Instead, for the [S II] line doublet, we find an intensity ratio [S II] $I(\lambda 6716)/I(\lambda 6731)$ ≈ 1.45 ± 0.05. For temperatures ~10^4 K, this ratio corresponds to the low-density limit, $n_e < 10$ cm^{-3}, consistent with the standard ISM density of ~1 cm^{-3}. Given the close proximity and similar environment of ULX-1 and ULX-2, it is plausible to assume that was also the unperturbed ISM density around ULX-1, before the gas was compressed by the shock front.

With log ([N II] $\lambda 6583$/Hα) ≈ -0.51, log ([S II] $\lambda 6716 + \lambda 6731$/H$\alpha$) ≈ -0.55, and log ([O III] $\lambda 5007$/Hα) ≈ -0.02, the nebula sits along the sequence of H II regions photoionized by stellar emission (Baldwin, Phillips & Terlevich 1981; Veilleux & Osterbrock 1987; Kewley & Dopita 2002). The lack of high-ionization lines such as He II $\lambda 4686$ and [Ne V] $\lambda 3426$ (detected in the ULX-1 nebula, Section 3.2.1) is further evidence that most of the ionizing photons come from the stellar population rather than the ULX. Non-detection of [O I] $\lambda 6300$ suggests the lack of an extended low-ionization zone, which we would expect to find if the nebulae were ionized by soft X-ray photons from ULX-2.

Using nitrogen and oxygen lines as metallicity indicators, we run into the well-known discrepancy (Kennicutt, Bresolin &
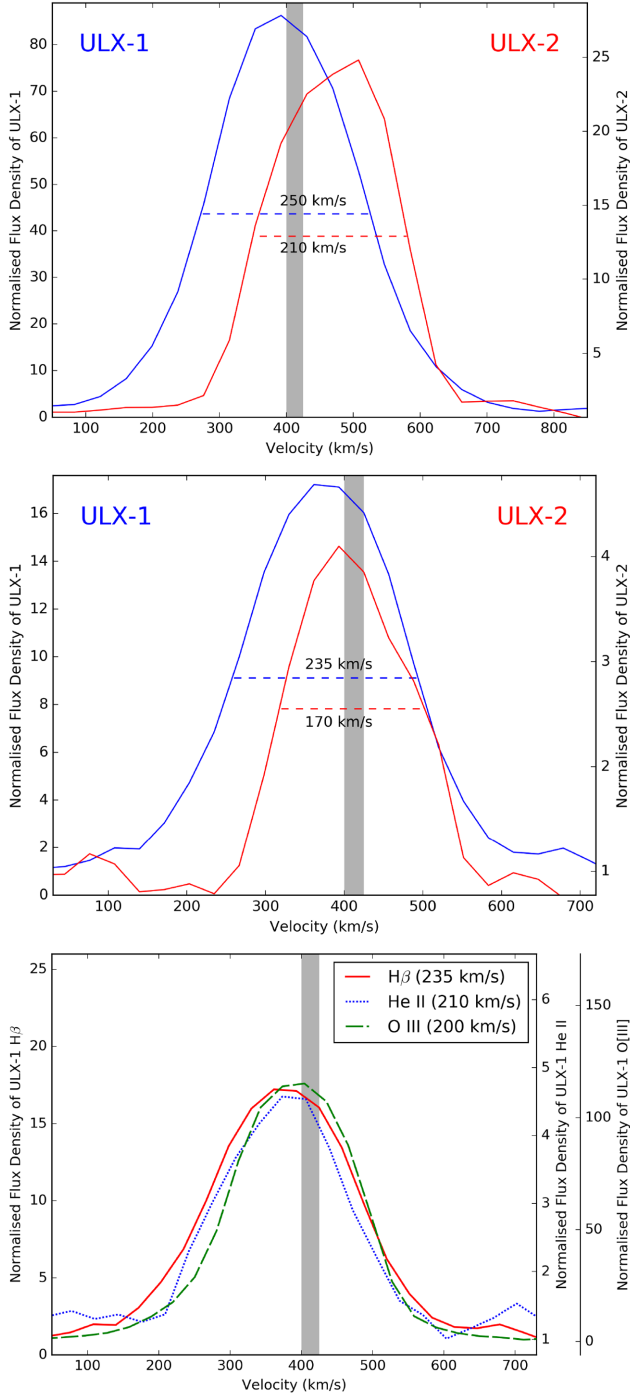
Figure 9. Top panel: Hα line profile for the nebulae around ULX-1 (blue) and around ULX-2 (red). The shaded band indicates the systemic velocity expected in the M 51 spiral arm at the location of ULX-1 and ULX-2 ($\approx$400–425 km s^{-1}, from Vlahakis et al. 2013 and Shetty et al. 2007). The FWHM of the two lines is also overplotted; both the FWHM and the FWZI are higher in the ULX-1 nebula. Middle panel: same as the top panel, but for the Hβ line; again, the line from the ULX-1 nebula is broader. Bottom panel: comparison between the line profiles of He II λ4686, [O III] λ5007, and Hβ (plotted with the same peak intensity for convenience) for the ULX-1 nebula: the relatively small FWHM and lack of broad wings in the higher-ionization lines are inconsistent with the high shock velocity that would be required to produce such lines entirely from shocks, and suggests a significant contribution to those lines from X-ray photoionization.

Garnett 2003; Bresolin, Garnett & Kennicutt 2004) between the 'direct' metallicity calibration based on oxygen temperatures, and the 'indirect' calibration based on photoionization models. The direct T_e-based measurements require detection of faint auroral lines (e.g. [O III] λ4363; Kennicutt et al. 2003), while photoionization models constrain the metal abundance from the intensity of stronger lines, for example the ratio between [N II] λ6584 and [O II] $\lambda\lambda$3726, 3729 (Kewley & Dopita 2002). It was noted (Bresolin et al. 2004) that indirect photoionization abundances of H II regions in nearby spiral galaxies are systematically higher than T_e-measured abundances by a factor of 2–3. For our present study, we cannot directly measure T_e abundances for the ULX-2 nebula; we have to rely on stronger lines (Table 2) and use either the direct or the indirect calibration between those line ratios and the metal abundance. Applying the T_e-based calibration, from our measured values of log ([N II] λ6583/Hα) and of log [([O III] λ5007/Hβ)/([N II] λ6583/Hα)] we find log (O/H) +12 $\approx$ 8.6 $\pm$ 0.1, that is about 20 per cent below solar (using the definition of solar abundance from Allende Prieto, Lambert & Asplund 2001). This is the same as the metal abundance directly measured for several other H II regions in the same spiral arm of M 51, at similar radial distances from the galactic nucleus (Bresolin et al. 2004; Croxall et al. 2015). On the other hand, based on the indirect calibration of Kewley & Dopita (2002), Kobulnicky & Kewley (2004), and Pilyugin & Thuan (2005), the same line ratios correspond to log (O/H) +12 $\approx$ 9.1 $\pm$ 0.1, that is $Z \approx 2.5 Z_\odot$. A similar discrepancy also occurs if we use the so-called R_{23} metallicity indicator, that is the intensity ratio between ([O II] $\lambda\lambda$3726, 3729 + [O III] $\lambda\lambda$4959, 5007) over Hβ (Pagel et al. 1979; Edmunds & Pagel 1984; Kewley & Dopita 2002; Kewley & Ellison 2008). The traditional calibration of this ratio based on photoionization models gives log (O/H) +12 $\approx$ 9.1, 3 times higher than the value derived from the direct measurements of Kennicutt et al. (2003) and Bresolin et al. (2004) (see in particular Fig. 7 in the latter paper). Previous work in the literature supporting a supersolar metallicity for the M 51 disc (Moustakas et al. 2010; Zaritsky et al. 1994) was also calibrated on photoionization models. Resolving the systematic discrepancy between the two metallicity calibrations will be important for population synthesis models of ULXs, because the ratio between neutron stars and black holes produced from stellar collapses increases strongly at supersolar metallicities (Heger et al. 2003).

3.3 Radio counterpart of ULX-1

The VLA+Effelsberg data show a faint radio source near ULX-1, detected both at 1.4 GHz and at 4.9 GHz, however not detected at 8.4 GHz. In the 1.4 and 4.9 GHz radio images the source is marginally resolved, elongated in the east–west direction (Fig. 10), that is the same long axis of the optical nebula. The position of the peak intensity in the radio source is slightly offset, by $\approx$1 arcsec, to the east of the *Chandra* position and of the central region of the ULX bubble in the *HST* image. Such an offset is significantly larger than the astrometric uncertainty (Section 2.4) of the X-ray and optical images. Thus, we speculate that the peak radio emission comes from a hotspot where the eastern jet interacts with the ISM, rather than being associated with the core. From the primary-beam corrected data, we determined peak brightnesses $f_{1.4\,\text{GHz}} = (44.8 \pm 9.2)$ μJy beam^{-1}, $f_{4.9\,\text{GHz}} = (29.8 \pm 7.3)$ μJy beam^{-1}, and an 8.4-GHz upper limit of $f_{8.4\,\text{GHz}} < 54$ μJy beam^{-1}. The integrated fluxes are $f_{1.4\,\text{GHz}} = (110 \pm 23)$ μJy and $f_{4.9\,\text{GHz}} = (52.7 \pm 12.4)$ μJy. At the distance of M 51, this corresponds to a 4.9-GHz
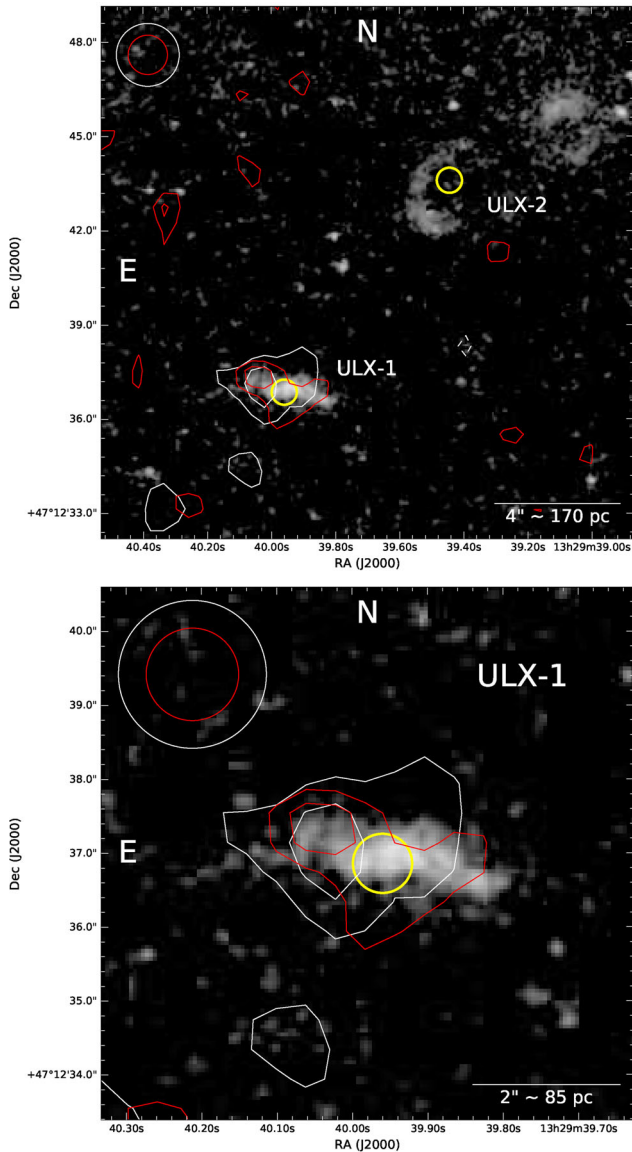
Figure 10. Top panel: *HST*/ACS continuum-subtracted F658N image of the ULX field, with VLA radio contours overplotted. White and red contours represent the 4.9- and 1.4-GHz flux densities, respectively. Both sets of contours have levels of $-2\sqrt{2}\sigma$, $2\sqrt{2}\sigma$, and 4σ, where σ is the respective noise level ($\sigma_{4.9} = 7.3$ μJy beam^{-1}, $\sigma_{1.4} = 9.2$ μJy beam^{-1}). Beams for both frequencies are indicated in the top left-hand corner of the image. The yellow circles represent the *Chandra* positions of ULX-1 and ULX-2 with 0.4 arcsec uncertainty. Bottom panel: zoomed-in view of the ULX-1 bubble.

luminosity[9] $L_{4.9\,\text{GHz}} = (2.3 \pm 0.5) \times 10^{34}$ erg s^{-1}. From the integrated fluxes, we determine a spectral index[10] $\alpha = -0.6 \pm 0.3$, consistent with the optically thin synchrotron emission expected from hot spots. Radio flux may also come from free–free emission associated with the ionized bubble; however, based on the Balmer emission, we only expect a free–free flux density of ≈ 1.5 μJy at 4.9 GHz (Caplan & Deharveng 1986, Appendix A), entirely negligible. The radio emission may also be a result of a supernova remnant; however, the highly elongated morphology of the optical nebula suggests

---

[9]The luminosity is defined as $L_\nu = 4\pi d^2 \nu f_\nu$.
[10]Defined as $f_\nu \propto \nu^\alpha$

that we are looking at a strongly collimated outflow, thus more likely driven by the ULX.

We do not detect any radio emission associated with ULX-2 or its surrounding nebula. We can only place 3σ upper limits on the peak flux densities: $f_{1.4\,\text{GHz}} < 28$ μJy beam^{-1}, $f_{4.9\,\text{GHz}} < 22$ μJy beam^{-1}, and $f_{8.4\,\text{GHz}} < 54$ μJy beam^{-1}. This corresponds to an upper limit to the 4.9-GHz luminosity $L_{4.9\,\text{GHz}} < 10^{34}$ erg s^{-1}. The expected free–free emission from the H II region around ULX-2 is ≈ 2 μJy at 4.9 GHz (Caplan & Deharveng 1986), well below the detection limit.

4 DISCUSSION

Although the X-ray luminosity of ULX-1 and ULX-2 is only moderately above 10^{39} erg s^{-1}, the two sources have interesting properties that can help us understand the behaviour of supercritical accretion. Both sources are eclipsing (Urquhart & Soria 2016b), showing sharp transitions in which the companion star occults the compact object. Eclipsing sources are very rare amongst ULXs and X-ray binaries in general. The presence of periodic eclipses enables a number of binary parameters to be constrained (e.g. binary period, inclination angle, mass function, and size of the X-ray emitting region). This makes these objects prime targets for follow-up multiwavelength observations. Here, we have shown that both ULXs are associated with ionized gas nebulae, with different optical spectral properties. We have also shown that ULX-1 (but not ULX-2) has a radio counterpart (usually taken as a signature of jet activity). We shall now discuss the physical interpretation of the sources, putting together the various clues from these multiband observations.

4.1 Energetics of the two nebulae

As we have shown in Section 3.2, the most obvious difference between the two nebulae is that one is dominated by shock ionization (with possible additional contribution from X-ray photoionization), the other by near-UV photoionization. We shall discuss here how much kinetic and radiative energy is required to produce the luminosity observed from the two nebulae, and whether the two ULXs are the origin of such power.

4.1.1 Mechanical power of ULX-1

From standard bubble theory (Weaver et al. 1977), the mechanical power P_{jet} inflating the bubble is equal to $\approx 77/27$ of the total radiative luminosity L_{rad}. The luminosity in the Hβ line ($L_{\text{H}\beta}$) is between $\approx 4 \times 10^{-3}$ and $\approx 7 \times 10^{-3}$ times the total radiative luminosity, for all shock velocities $100 \lesssim v_s \lesssim 500$ km s^{-1} (from the set of pre-run shock-ionization MAPPINGS III models for equipartition magnetic field and either solar or twice-solar abundance; Allen et al. 2008). Thus, $P_{\text{jet}} \approx (400$–$650) \times L_{\text{H}\beta}$. Knowing that $L_{\text{H}\beta} \approx 3.7 \times 10^{36}$ erg s^{-1}, we infer a mechanical power $P_{\text{jet}} \approx (1.5$–$2.5) \times 10^{39}$ erg s^{-1}. This value is comparable to the X-ray luminosity of ULX-1 (Urquhart & Soria 2016b), taking into account the uncertainty in the viewing angle and therefore the geometric projection factor for the disc emission. It is also similar to the jet power inferred for SS 433 (Fabrika 2004; Panferov 2017). There is no direct conversion between jet power and luminosity of the radio counterpart because the latter also depends on other factors such as the ISM density and magnetic field, and the fraction of kinetic power carried by protons and ions; however, it is interesting to note that the 5-GHz luminosity $L_{4.9\,\text{GHz}} \approx 2.3 \times 10^{34}$ erg s^{-1} is within a factor of 2 of the radio luminosity of other jetted ULXs such as Holmberg II

X-1 (Cseh et al. 2014, 2015) and NGC 5408 X-1 (Soria et al. 2006; Lang et al. 2007; Cseh et al. 2012). Thus, the radio luminosity of the M 51 ULX-1 nebula seems to correspond to 'average' jetted ULX properties: it is a factor of 5 more radio luminous than SS 433, but an order of magnitude fainter than the most exceptional radio bubbles in the local universe, namely NGC 7793 S26 (Pakull et al. 2010; Soria et al. 2010) and IC 342 X-1 (Cseh et al. 2012), which are also a few times larger. The radio spectral index $\alpha = -0.6 \pm 0.3$ confirms that the radio counterpart is dominated by optically thin synchrotron emission, as expected for jet lobes.

An alternative method to estimate the jet power (Weaver et al. 1977) is to assume that the moderate shock velocity $\approx$100–150 km s^{-1} inferred from the FWHM of the Balmer lines also corresponds to the advance speed of the jet-powered forward shock into the ISM. In that scenario, the characteristic age of the bubble is $\approx 3 \times 10^5 v_{100}^{-1}$ yr and the jet power $P_{jet} \approx 1.0 \times 10^{39} v_{100}^3 n_e$ erg s^{-1}, where $v_{100} \equiv v_s/(100\,\mathrm{km\,s^{-1}})$ and n_e is the ISM number density. This is consistent with the other jet power estimate.

There is clearly a strong discrepancy between the moderately low FWHM of all the lines ($\sim$100 km s^{-1}) and the high shock velocity ($\sim$500 km s^{-1}) that would be needed to produce the higher ionization lines with the observed ratios; such high shock velocities are also inconsistent with the observed HWZIs and the moderate gas temperature inferred from the [S II] lines. Even if we account for the fact that about half of the high-ionization line emission occurs in the precursor region (low turbulent velocity), the discrepancy remains difficult to explain. One possibility is that there is a contribution from X-ray photoionization, from ULX-1. The source appears almost edge-on to us, but if, as expected, its polar funnel is aligned with the major axis of the bubble (i.e. along the jet), there is stronger direct X-ray irradiation and lower intrinsic absorption along that direction. The fact that high-ionization lines are slightly narrower than low-ionization lines supports the idea that the former are partly enhanced by X-ray photoionization. Another possibility is that the shocked gas does have a faster expansion velocity (comparable with the shock velocity) along the direction of the jet (which is located approximately in the plane of the sky for us) and a slower expansion in the other two directions perpendicular to the jet axis; in that case, the line width observed by us only reflects the lateral expansion speed. Soft thermal X-ray emission is a possible test for the presence of fast shocks: a shock velocity $\approx$500 km s^{-1} corresponds to a shock temperature $\approx$0.3 keV. Soft thermal emission was indeed detected in the X-ray spectrum of ULX-1 (Urquhart & Soria 2016b); unfortunately, the location of the source away from the aimpoint in the *Chandra* observations, and the low spatial resolution of *XMM–Newton*, do not enable us to determine whether the thermal-plasma component comes only from the central point-like source or from the larger bubble. In the former case, the X-ray line emission would be directly linked to the disc outflow around the ULX; in the latter case, it would be from the jet/ISM interaction. New *Chandra* observations with the source at the aimpoint could answer this question.

4.1.2 Radiative power of ULX-2

The optical spectrum of the nebula around ULX-2 is consistent with a typical H II region; this would mean that it is only a coincidence that a ULX is apparently located inside the nebula, without contributing to its ionization. To determine whether this is the case, we start by measuring its extinction-corrected Hβ luminosity: $L_{H\beta} \approx 4.0 \times 10^{36}$ erg s^{-1}. At $T_e \approx 10\,000$ K, the emission of one Hβ

photon requires $\approx$8.5 ionizing photons above 12.6 eV (Osterbrock 1989), and below $\approx$0.2 keV (above which energy the ionization cross-section becomes too low). Therefore, the observed nebular luminosity implies an ionizing photon flux $Q(H^0) \approx 8 \times 10^{48}$ photons s^{-1}. From the best-fitting parameters in the solar-metallicity stellar tracks, we estimate that the two blue stars in the error circle of ULX-2 have effective temperatures of $\approx$20 000 K and $\approx$17 000 K, and radii of $\approx$25 R$_\odot$ and $\approx$36 R$_\odot$, respectively. Approximating the spectra of the two stars as blackbodies, we expect a combined ionizing flux of $\approx 1.4 \times 10^{48}$ photons s^{-1} above 12.6 eV. Adding a few other blue stars inside the outer boundary of the nebula still leaves us a factor of 3 short of the required ionizing flux. However, using only the bright blue supergiants for this type of photon accounting can be misleading. For example, the addition of a single main-sequence mid-type O star (O6V or O7V), with a temperature $\approx$35 000–37 000 K, would suffice to provide the remaining ionizing flux (Simón-Díaz & Stasińska 2008). Such O-type dwarfs have an absolute brightness $M_V \approx -4.5$ mag, negligible compared with the characteristic absolute brightness $M_V \approx -6$ mag of the B4–B6 supergiants around ULX-2. Thus, if one of the four supergiants visible around ULX-2 (Fig. 2, bottom right) is in a binary system with a mid-type O star, the supergiants will determine the optical colours and V-band luminosity, but the O star will provide most of the ionizing UV flux. Another way to tackle the problem is to use STARBURST99 (Leitherer et al. 1999, 2014) simulations: we find that for a single population age of 7 Myr, a stellar mass of $\approx 10^4$ M$_\odot$ would be required to provide the necessary ionizing flux. Adding a dust reddening correction for the M 51 halo (as discussed in Sections 2.2 and 3.1) would increase the intrinsic ionizing luminosity of the stars by $\approx$50 per cent, making it easier to meet the energy requirements for the H II region.

Estimating whether there may also be a direct photoionizing contribution from ULX-2 is not trivial. The X-ray source is seen at a high inclination angle θ, which implies that an isotropic conversion of observed high-energy flux into emitted luminosity may underestimate the disc emission; a conversion factor of $\approx 2\pi d^2/\cos\theta$ is more appropriate than a factor of $4\pi d^2$. Taking this into account, we can always find a sufficiently high viewing angle (in particular, $\theta \gtrsim 80°$) to increase the true emitted disc luminosity of the source. To boost the number of UV photons, we must also assume that the X-ray source is surrounded by a large disc that intercepts and reprocesses more than 1 per cent of the X-ray flux. Thus, an ionizing flux $Q(H^0) \approx 8 \times 10^{48}$ photons s^{-1} is consistent with the X-ray and optical luminosity of ULX-2. However, the problem of this irradiated-disc scenario is that it also produces copious amount of photons at energies >54 eV, which leads to the emission of He II $\lambda 4686$ via recombination of He^{++} into He$^+$. No He II $\lambda 4686$ emission is detected in the LBT spectra of the nebula, with an upper limit on its flux of $\approx 10^{-16}$ erg cm^{-2} s^{-1}, corresponding to an emitted photon flux $\lesssim 2 \times 10^{47} \lambda 4686$ photons s^{-1}. At $T_e \sim 10\,000$ K, it takes $\approx$4.2 primary ionizing photons >54 eV to produce one $\lambda 4686$ photon (Pakull & Angebault 1986; Osterbrock 1989): thus, the flux of $E > 54$ eV photons seen by the nebular gas must be $\lesssim 8 \times 10^{47}$ photons s$^{-1} \approx 0.1 Q(H^0)$. Typical models of irradiated discs (e.g. *diskir* in XSPEC) luminous enough to produce the required number of photons >13.6 eV will also predict too many photons >54 eV (typically, the latter are predicted to be $\approx$1/4 of the former, rather than $\lesssim$1/10, as required by the observed spectrum). Given this evidence, we conclude that the ionized nebula projected around ULX-2 is a typical H II region and the ULX, whether located inside the nebula or not, is not its major ionizing source.

4.2 Radio brighter and radio fainter ULX bubbles

ULX bubbles are a crucial tool to estimate the emitted power (radiative and kinetic luminosity) of the compact object, averaged over the characteristic cooling time-scale of the gas. Moreover, they enable us to identify compact objects with likely supercritical accretion that currently appear X-ray faint, either because they are in a low state, or because they are collimated away from us, or because the direct X-ray emission along our line of sight is blocked by optically thick material. As more ULX bubbles get discovered or recognized, we are starting to see that there is no simple correlation between the X-ray luminosity of the central source and the radio or Balmer line luminosity of the bubble. The differences between M 51 ULX-1 and ULX-2 illustrated in this paper are a clear example. This is also the case when we compare the M 51 ULX-1 bubble with ULX bubbles in other galaxies. For example, the collisionally ionized ULX bubble around Holmberg IX X-1 (Pakull & Mirioni 2002; Abolmasov & Moiseev 2008; Pakull & Grisé 2008; Grisé et al. 2011) has an H α luminosity $\approx 10^{38}$ erg s^{-1} (Miller & Hodge 1994; Miller 1995; Abolmasov & Moiseev 2008), an order of magnitude higher than that of the M 51 ULX-1 bubble, consistent with a mechanical power of $\approx 10^{40}$ erg s^{-1}; the central ULX powering the Holmberg IX bubble has an X-ray luminosity $L_X \approx 2 \times 10^{40}$ erg s^{-1} (Walton et al. 2017 and references therein), again an order of magnitude higher than M 51 ULX-1. However, the Holmberg IX ULX bubble has a 1.4-GHz luminosity of $\approx 2 \times 10^{34}$ erg s^{-1} (our estimate based on the radio maps of Krause, Beck & Hummel 1989), similar to the radio luminosity of M 51 ULX-1. Conversely, there are ULXs with more luminous radio nebulae (such as Holmberg II X-1 and NGC 5408 X-1; see Section 4.1.1 for references) and proof of powerful jets, but with relatively weak or no collisionally ionized gas detectable from optical lines. The different ratio of synchrotron radio luminosity over mechanical power (or radio luminosity over total accretion power) in different ULXs may be due to various factors: (i) a different initial kinetic energy distribution between a collimated, relativistic jet and a slower, more massive disc wind; (ii) different composition of the jet (leptonic or baryonic); (iii) different amount of entrainment of ISM matter along the jet path (related to different ISM densities). A general classification of ULX bubbles in terms of their multiband luminosity ratios is beyond the scope of this work.

For the ULXs that do show radio evidence of extended jets, typical 5-GHz luminosities span an order of magnitude between $\approx 2 \times 10^{34}$ erg s^{-1} in M 51 ULX-1 and $\approx 2 \times 10^{35}$ erg s^{-1} in NGC 7793-S26 (Soria et al. 2010) and IC 342 X-1 (Cseh et al. 2012); the characteristic age of the ULX bubbles is $\sim$ a few 10^5 yr. This luminosity range corresponds to a range of observed fluxes $f_{5\mathrm{GHz}} \approx (30\text{--}300) \, d_{10}^{-2} \, \mu$Jy, where d_{10} is the source distance in units of 10 Mpc. The synchrotron radio flux observed from microquasar lobes during the active expansion phase, that is when the jet is still inflating them, was modelled by Heinz (2002) as $f_{5\mathrm{GHz}} \sim 10 \, n_e^{0.45} \, P_{\mathrm{jet},39}^{1.3} \left[2\varphi^{3/4}/(1+\varphi) \right] t_5^{0.4} \, d_{10}^{-2}$ mJy, where φ is the ratio between the magnetic pressure and the gas pressure at the base of the jet, $P_{\mathrm{jet}, 39}$ is the jet power in units of 10^{39} erg s^{-1}, t_5 is the age of the jet active phase in units of 10^5 yr, and n_e is the number density in the ISM. While the Heinz (2002) scaling relation works well for the radio nebula around the neutron star microquasar Cir X-1, it overestimates the synchrotron radio luminosity of the bubble around the BH microquasar Cyg X-1 by at least two orders of magnitude Gallo et al. (2005); it also overestimates the synchrotron radio luminosity of ULX bubbles (given the input mechanical power inferred from line-emission studies) by a similar amount. For Cyg

X-1, this may be the result of a significant fraction of the jet energy being stored in baryons that do not radiate (Gallo et al. 2005; Heinz 2006). A similar explanation may apply to jet-driven ULX bubbles (Soria et al. 2010).

5 CONCLUSIONS

We presented the discovery and multiband study of two ionized nebulae spatially associated with the two eclipsing ULXs in M 51, using new and archival data from *Chandra*, the LBT, the *HST*, and the VLA. The nebula around ULX-1 has a very elongated morphology, indicative of a jet-driven bubble. We showed that the optical emission lines are collisionally ionized and that there is a spatially resolved radio counterpart. Such findings are consistent with the jet interpretation. We know from X-ray photometry that ULX-1 is seen almost edge-on; therefore, the jet is likely propagating in the plane of the sky, which explains the lack of systemic velocity shifts observed between the eastern and western ends of the optical bubble. The mechanical power of the jet estimated from the H β luminosity, $P_{\mathrm{jet}} \approx 2 \times 10^{39}$ erg s^{-1}, agrees with the power estimated from the FWHM of the lines (proportional to the shock velocity) and the characteristic age of the source ($t \sim 10^5$ yr). However, high-ionization lines (specifically, [Ne v] λ3426, He II λ4686, and a few [O III] lines) are too strong for the shock velocity $v_s \sim 100\text{--}150$ km s^{-1} inferred from the width of the low-ionization lines. Either there is also a shock component with $v_s \sim 500$ km s^{-1}, or the high-ionization lines are boosted by X-ray photoionization. We favour the latter scenario because the high-ionization lines are slightly narrower than the Balmer lines.

Conversely, the nebula around ULX-2 has a quasi-circular appearance and its line ratios and widths are consistent with a normal H II region, that is with stellar photoionization from one or two O-type dwarfs and a few blue supergiants. There is no radio counterpart and no other evidence of jet emission. The reason why some ULXs produce jets while others (with comparable X-ray luminosities) do not, both in the case of the two M 51 sources and in the ULX class as a whole remains unknown. The lack of high-ionization lines indicative of X-ray photoionization suggests that ULX-2 does not have a strong direct contribution to the ionization of the nebula. It is likely that the nebula is a chance alignment and is not powered by the ULX.

The X-ray and multiband flux from the two compact objects and surrounding nebulae is at the low end of the ULX class distribution; however, the peculiar property of both sources is that they show X-ray eclipses, from which one can in principle strongly constrain the binary parameters, the masses of the two compact objects, and the geometry of accretion and emission. Therefore, they are particularly suitable targets for follow-up multiband studies.

The metallicity of the parent stellar population can have a direct effect on the type of ULXs and on their observational appearance. For example at supersolar metallicities, the ratio of neutron stars over black holes is strongly increased, which may be relevant to the ongoing debate over the relative proportion of neutron star and black hole accretors in the ULX population. Neutron stars with a Roche lobe-filling massive donor star are also more likely to be eclipsing systems than black holes with the same type of donor star, which may explain why two eclipsing ULXs (Urquhart & Soria 2016b) and another eclipsing X-ray binary with a luminosity just below the ULX threshold (Wang et al. in preparation) were all found in this galaxy. Our LBT spectra of the ionized gas around ULX-2 are in agreement with the line ratios observed in previous

optical studies of H II regions in the disc of M 51 (as discussed in Section 3.2.2); however, the conversion between such line ratios and a metallicity scale remains a subject of debate, with alternative models suggesting either $Z \approx 0.015$ (slightly sub-solar) or $Z \approx 0.04$ (2.5 times supersolar). Future, more accurate, determinations of the metallicity in nearby spiral galaxies will provide an important input parameter to test population synthesis models of ULXs.

ACKNOWLEDGEMENTS

REFERENCES

Abolmasov P., Moiseev A. V., 2008, Rev. Mex. Astron. Astrofis., 44, 301
Allen M. G., Groves B. A., Dopita M. A., Sutherland R. S., Kewley L. J., 2008, ApJS, 178, 20
Allende Prieto C., Lambert D. L., Asplund M., 2001, ApJ, 556, L63
Bachetti M. et al., 2014, Nature, 514, 202
Baldwin J. A., Phillips M. M., Terlevich R., 1981, PASP, 93, 5
Begelman M. C., Blandford R. D., Rees M. J., 1984, Rev. Mod. Phys., 56, 255
Blair W. P., Long K. S., 1997, ApJS, 108, 261
Bohlin R. C., 2016, AJ, 152, 60
Boumis P. et al., 2007, MNRAS, 381, 308
Bresolin F., Garnett D. R., Kennicutt R. C., Jr, 2004, ApJ, 615, 228
Bressan A., Marigo P., Girardi L., Salasnich B., Dal Cero C., Rubele S., Nanni A., 2012, MNRAS, 427, 127
Brinkmann W., Pratt G. W., Rohr S., Kawai N., Burwitz V., 2007, A&A, 463, 611
Caplan J., Deharveng L., 1986, A&A, 155, 297
Cardelli J. A., Clayton G. C., Mathis J. S., 1989, ApJ, 345, 245
Chen Y., Bressan A., Girardi L., Marigo P., Kong X., Lanza A., 2015, MNRAS, 452, 1068
Croxall K. V., Pogge R. W., Berg D. A., Skillman E. D., Moustakas J., 2015, ApJ, 808, 42
Cseh D. et al., 2012, ApJ, 749, 17
Cseh D. et al., 2014, MNRAS, 439, L1
Cseh D. et al., 2015, MNRAS, 452, 24

de Jong J. A., van Paradijs J., Augusteijn T., 1996, A&A, 314, 484
Dopita M. A., Sutherland R. S., 2003, Astrophysics of the diffuse universe
Dubner G. M., Holdaway M., Goss W. M., Mirabel I. F., 1998, AJ, 116, 1842
Dubus G., Lasota J.-P., Hameury J.-M., Charles P., 1999, MNRAS, 303, 139
Dumas G., Schinnerer E., Tabatabaei F. S., Beck R., Velusamy T., Murphy E., 2011, AJ, 141, 41
Edmunds M. G., Pagel B. E. J., 1984, MNRAS, 211, 507
Eggleton P. P., 1983, MNRAS, 204, 449
Fabrika S., 2004, Astrophys. Space Phys. Rev., 12, 1
Farnes J. S., Gaensler B. M., Purcell C., Sun X. H., Haverkorn M., Lenc E., O'Sullivan S. P., Akahori T., 2017, MNRAS, 467, 4777
Farrell S. A., Webb N. A., Barret D., Godet O., Rodrigues J. M., 2009, Nature, 460, 73
Feng H., Soria R., 2011, New A Rev., 55, 166
Fruscione A. et al., 2006, Proc. SPIE, 6270, 62701V
Fürst F. et al., 2016, ApJ, 831, L14
Fürst F., Walton D. J., Stern D., Bachetti M., Barret D., Brightman M., Harrison F. A., Rana V., 2017, ApJ, 834, 77
Gallo E., Fender R., Kaiser C., Russell D., Morganti R., Oosterloo T., Heinz S., 2005, Nature, 436, 819
Gandhi P. et al., 2010, MNRAS, 407, 2166
Gierliński M., Done C., Page K., 2009, MNRAS, 392, 1106
Gladstone J. C., Copperwheat C., Heinke C. O., Roberts T. P., Cartwright T. F., Levan A. J., Goad M. R., 2013, ApJS, 206, 14
Goodall P. T., Alouani-Bibi F., Blundell K. M., 2011, MNRAS, 414, 2838
Gordon S. M., Kirshner R. P., Long K. S., Blair W. P., Duric N., Smith R. C., 1998, ApJS, 117, 89
Greisen E. W., 2003, Information Handling in Astronomy - Historical Vistas, 285, 109
Grisé F., Pakull M. W., Motch C., 2006, in Meurs E. J. A., Fabbiano G., eds., Proc. IAU Symp. 230, Populations of High Energy Sources in Galaxies. Cambridge Univ. Press, Cambridge, p. 302
Grisé F., Kaaret P., Pakull M. W., Motch C., 2011, ApJ, 734, 23
Grisé F., Kaaret P., Corbel S., Feng H., Cseh D., Tao L., 2012, ApJ, 745, 123
Hack W. J., Greenfield P., 2000, in Manset N., Veillet C., Crabtree D., eds., ASP Conf. Ser., Vol. 216, Astronomical Data Analysis Software and Systems IX. Astron. Soc. Pac., San Francisco, p. 433
Heger A., Fryer C. L., Woosley S. E., Langer N., Hartmann D. H., 2003, ApJ, 591, 288
Heida M. et al., 2014, MNRAS, 442, 1054
Heinz S., 2002, A&A, 388, L40
Heinz S., 2006, ApJ, 636, 316
Hynes R. I., Haswell C. A., Chaty S., Shrader C. R., Cui W., 2002, MNRAS, 331, 169
Israel G. L. et al., 2017a, Science, 355, 817
Israel G. L. et al., 2017b, MNRAS, 466, L48
Izotov Y. I., Thuan T. X., Privon G., 2012, MNRAS, 427, 1229
Joye W. A., Mandel E., 2003, in Payne H. E., Jedrzejewski R. I., Hook R. N., eds., ASP Conf. Ser. Vol. 295, Astronomical Data Analysis Software and Systems XII. Astron. Soc. Pac., San Francisco, p. 489
Kaaret P., Corbel S., 2009, ApJ, 697, 950
Kaaret P., Corbel S., Prestwich A. H., Zezas A., 2003, Science, 299, 365
Kaaret P., Feng H., Wong D. S., Tao L., 2010, ApJ, 714, L167
Kaaret P., Feng H., Roberts T. P., 2017, ARA&A, 55, 303
Kennicutt R. C., Jr, Bresolin F., Garnett D. R., 2003, ApJ, 591, 801
Kewley L. J., Dopita M. A., 2002, ApJS, 142, 35
Kewley L. J., Ellison S. L., 2008, ApJ, 681, 1183
King A. R., Kolb U., Szuszkiewicz E., 1997, ApJ, 488, 89
Kobulnicky H. A., Kewley L. J., 2004, ApJ, 617, 240
Krause M., Beck R., Hummel E., 1989, A&A, 217, 17
Lang C. C., Kaaret P., Corbel S., Mercer A., 2007, ApJ, 666, 79
Leitherer C. et al., 1999, ApJS, 123, 3
Leitherer C., Ekström S., Meynet G., Schaerer D., Agienko K. B., Levesque E. M., 2014, ApJS, 212, 14
Liu J.-F. et al., 2015, Nature, 528, 108
Mathewson D. S., Clarke J. N., 1973, ApJ, 180, 725

McQuinn K. B. W., Skillman E. D., Dolphin A. E., Berg D., Kennicutt R., 2016, ApJ, 826, 21

Mezcua M., Farrell S. A., Gladstone J. C., Lobanov A. P., 2013a, MNRAS, 436, 1546

Mezcua M., Roberts T. P., Sutton A. D., Lobanov A. P., 2013b, MNRAS, 436, 3128

Mezcua M., Roberts T. P., Lobanov A. P., Sutton A. D., 2015, MNRAS, 448, 1893

Middleton M. J. et al., 2013, Nature, 493, 187

Middleton M. J., Walton D. J., Fabian A., Roberts T. P., Heil L., Pinto C., Anderson G., Sutton A., 2015, MNRAS, 454, 3134

Miller B. W., 1995, ApJ, 446, L75

Miller B. W., Hodge P., 1994, ApJ, 427, 656

Moustakas J., Kennicutt R. C., Jr, Tremonti C. A., Dale D. A., Smith J.-D. T., Calzetti D., 2010, ApJS, 190, 233

Narayan R., Sądowski A., Soria R., 2017, MNRAS, 469, 2997

Ohsuga K., Mineshige S., 2011, ApJ, 736, 2

Ohsuga K., Mori M., Nakamoto T., Mineshige S., 2005, ApJ, 628, 368

Osterbrock D. E., 1989, Astrophysics of Gaseous Nebulae and Active Galactic Nuclei. University Science Books, Mill Valley, CA

Osterbrock D. E., Ferland G. J., 2006, Astrophysics of Gaseous Nebulae and Active Galactic Nuclei. University Science Books, Sausalito, CA

Pagel B. E. J., Edmunds M. G., Blackwell D. E., Chun M. S., Smith G., 1979, MNRAS, 189, 95

Pakull M. W., Angebault L. P., 1986, Nature, 322, 511

Pakull M. W., Grisé F., 2008, in Bandyopadhyay R. M., Wachter S., Gelino D., Gelino C. R., eds., AIP Conf. Seri. Vol. 1010, A Population Explosion: The Nature & Evolution of X-ray Binaries in Diverse Environments. Am. Inst. Phys., New York, p. 303

Pakull M. W., Mirioni L., 2002, preprint (arXiv:astro-ph/0202488)

Pakull M. W., Mirioni L., 2003, in Arthur J., Henney W. J., eds., Rev. Mex. Astron. Astrofis. Conf. Ser. Vol. 15, Winds, Bubbles, and Explosions: a conference to honor John Dyson. Instituto de Astronomía, Univ. Nac. Auton. Mex., Mexico, p. 197

Pakull M. W., Grisé F., Motch C., 2006, in Meurs E. J. A., Fabbiano G., eds., Proc. IAU Symp. 230, Populations of High Energy Sources in Galaxies. Cambridge Univ. Press, Cambridge, p. 293

Pakull M. W., Soria R., Motch C., 2010, Nature, 466, 209

Panferov A. A., 2017, A&A, 599, A77

Pilyugin L. S., Thuan T. X., 2005, ApJ, 631, 231

Pinto C., Middleton M. J., Fabian A. C., 2016, Nature, 533, 64

Pogge R. W. et al., 2010, in McLean I. S., Ramsay S. K., Takami H., eds, Proc. SPIEConf. Ser. Vol. 7735, Ground-based and Airborne Instrumentation for Astronomy III. SPIE, Bellingham, p. 77350A

Poutanen J., Lipunova G., Fabrika S., Butkevich A. G., Abolmasov P., 2007, MNRAS, 377, 1187

Roberts T. P., Colbert E. J. M., 2003, MNRAS, 341, L49

Russell T. D., Soria R., Miller-Jones J. C. A., Curran P. A., Markoff S., Russell D. M., Sivakoff G. R., 2014, MNRAS, 439, 1390

Schlafly E. F., Finkbeiner D. P., 2011, ApJ, 737, 103

Shaw R. A., Dufour R. J., 1994, in Crabtree D. R., Hanisch R. J., Barnes J., eds., ASP Conf. Ser. Vol. 61, Astronomical Data Analysis Software and Systems III. Astron. Soc. Pac., San Francisco, p. 327

Shetty R., Vogel S. N., Ostriker E. C., Teuben P. J., 2007, ApJ, 665, 1138

Simón-Díaz S., Stasińska G., 2008, MNRAS, 389, 1009

Skrutskie M. F. et al., 2006, AJ, 131, 1163

Soria R., Kong A., 2016, MNRAS, 456, 1837

Soria R., Fender R. P., Hannikainen D. C., Read A. M., Stevens I. R., 2006, MNRAS, 368, 1527

Soria R., Pakull M. W., Broderick J. W., Corbel S., Motch C., 2010, MNRAS, 409, 541

Soria R., Kuntz K. D., Winkler P. F., Blair W. P., Long K. S., Plucinsky P. P., Whitmore B. C., 2012, ApJ, 750, 152

Soria R., Long K. S., Blair W. P., Godfrey L., Kuntz K. D., Lenc E., Stockdale C., Winkler P. F., 2014, Science, 343, 1330

Stetson P. B., 1987, PASP, 99, 191

Sutton A. D., Done C., Roberts T. P., 2014, MNRAS, 444, 2415

Swartz D. A., Ghosh K. K., Suleimanov V., Tennant A. F., Wu K., 2002, ApJ, 574, 382

Tao L., Feng H., Grisé F., Kaaret P., 2011, ApJ, 737, 81

Tao L., Kaaret P., Feng H., Grisé F., 2012, ApJ, 750, 110

Tody D., 1993, in Hanisch R. J., Brissenden R. J. V., Barnes J., eds., ASP Conf. Ser. Vol. 52, Astronomical Data Analysis Software and Systems II. Astron. Soc. Pac., San Francisco, p. 173

Urquhart R., Soria R., 2016a, MNRAS, 456, 1859

Urquhart R., Soria R., 2016b, ApJ, 831, 56

van Dyk S. D., Sramek R. A., Weiler K. W., Hyman S. D., Virden R. E., 1994, ApJ, 425, L77

Veilleux S., Osterbrock D. E., 1987, ApJS, 63, 295

Vlahakis C., van der Werf P., Israel F. P., Tilanus R. P. J., 2013, MNRAS, 433, 1837

Vrtilek S. D., Raymond J. C., Garcia M. R., Verbunt F., Hasinger G., Kurster M., 1990, A&A, 235, 162

Walton D. J. et al., 2017, ApJ, 839, 105

Warmels R. H., 1992, in Worrall D. M., Biemesderfer C., Barnes J., eds., ASP Conf. Ser. Vol. 25, Astronomical Data Analysis Software and Systems I. Astron. Soc. Pac., San Francisco, p. 115

Weaver R., McCray R., Castor J., Shapiro P., Moore R., 1977, ApJ, 218, 377

Zaritsky D., Kennicutt R. C., Jr, Huchra J. P., 1994, ApJ, 420, 87

Zealey W. J., Dopita M. A., Malin D. F., 1980, MNRAS, 192, 731

This paper has been typeset from a TeX/LaTeX file prepared by the author.